Available online at www.sciencedirect.com
ScienceDirect
European Journal of Mechanics B/Fluids 27 (2008) 726–749

Dynamics and bifurcations in the weak electrolyte model for electroconvection of nematic liquid crystals: a Ginzburg–Landau approach

Iuliana Oprea *, Gerhard Dangelmayr

Department of Mathematics, Colorado State University, Fort Collins, CO 80523, USA

Received 23 May 2007; received in revised form 1 December 2007; accepted 19 December 2007

Available online 21 February 2008

Abstract

In this paper we present the results of a bifurcation study of the weak electrolyte model for nematic electroconvection, for values of the parameters including experimentally measured values of the nematic I52. The linear stability analysis shows the existence of primary bifurcations of Hopf type, involving normal as well as oblique rolls. The weakly nonlinear analysis is performed using four globally coupled complex Ginzburg–Landau equations for the waves' envelopes. If spatial variations are ignored, these equations reduce to the normal form for a Hopf bifurcation with $O(2) \times O(2)$ symmetry. A rich variety of stable waves, as well as more complex spatiotemporal dynamics is predicted at onset. A temporal period doubling route to spatiotemporal chaos, corresponding to a period doubling cascade towards a chaotic attractor in the normal form, is identified. Eckhaus stability boundaries for travelling waves are also determined. The methods developed in this paper provide a systematic investigation of nonlinear physical mechanisms generating the patterns observed experimentally, and can be generalized to any two-dimensional anisotropic systems with translational and reflectional symmetry.

Keywords: Nematic electroconvection; Weak electrolyte model; Amplitude equations; Hopf bifurcation; Spatiotemporal chaos; Eckhaus stability

1. Introduction

A physical system serving as testing ground for many experimental studies and theoretical predictions of pattern formation in spatially extended systems is the electroconvection in nematic liquid crystals [1–3]. Nematic electroconvection provides a rich variety of pattern formation phenomena and has become a main paradigm for the study of anisotropic dissipative structures. From the experimental point of view, nematic electroconvection is attractive because of the easily accessible control parameters, the amplitude and the frequency of the applied voltage.

Nematic liquid crystals differ from ordinary, isotropic liquids by the fact that their molecules are on average locally oriented along a preferred direction, called the director. For electroconvection, the nematic is sandwiched between two glass plates, treated to produce planar (parallel to the glass plates) alignment of the director and an

* Corresponding author.
E-mail addresses: juliana@math.colostate.edu, ojuliana@yahoo.com (I. Oprea).

0997-7546/$ – see front matter
doi:10.1016/j.euromechflu.2007.12.004

electric potential difference is applied across the electrode plates. Above a critical value of the applied voltage an electrohydrodynamic instability combined with a transition from the uniform state to a variety of patterns can occur [4]. At onset one typically observes periodic patterns of convection rolls – normal or oblique rolls, depending on the frequency. With increasing voltage transitions take place either to complex spatiotemporal states, induced by defects, or to more complicated quasi-periodic patterns (see [1,3] for a recent review). For the nematics MBBA (*4-methyloxybenzylidene-4′-n-butyl-aniline*) and *I*52 (4-*ethyl*-2-*fluoro*-4'-[2-(*trans*-4-*pentylcyclohexyl*)-*ethyl*]*biphenyl*) complex spatiotemporal patterns, including localized structures and spatiotemporal chaos, have been detected even at onset, which provide a new challenge for the theory [5–8].

The traditionally used mathematical model to describe the electrohydrodynamic instability in nematic liquid crystals is the so-called standard model (SM) [9–11], that combines the continuum theory of Ericksen and Leslie for an electrically conducting anisotropic fluid with the quasistatic Maxwell equations, in the hypothesis that the charge conduction in the liquid crystal is ohmic. The SM is capable to capture several phenomena observed near threshold of *ac*-driven electroconvection in planar aligned nematic liquid crystals (e.g. normal, oblique and dielectric rolls, the structure and dynamics of defects), however, it does not exhibit an oscillatory instability which gives rise to the travelling wave patterns frequently observed near onset, and cannot explain the slightly subcritical nature of the bifurcation in some materials under certain conditions. Since experiments have shown that the electrical conductivity of nematics is non-ohmic [12], this suggested that the dynamics of ion recombination and dissociation may play a significant role in this system and led to the development of the weak electrolyte model (WEM) [13–15].

The WEM is an extension of the standard model, in which a slow dissociation-recombination of the current-carrying ions is taken into account and the ohmic behavior is replaced by the dynamics of two species of oppositely charged mobile ions. This additional process requires to treat the local conductivity σ as a further dynamic variable, and can lead to a distinctive change of the threshold behavior of the electrohydrodynamic instability.

One of the most important aspects of the WEM is the presence of a Hopf bifurcation that predicts the travelling wave patterns observed frequently near onset in experiments. The Hopf bifurcation can be explained physically as follows. In the SM the primary instability is caused by charge accumulation when the director is bend, which in turn leads to an increase in the electric field strength and hence to further bending of the director. In the WEM the migration of the charge carriers, described by the equation for σ, induces a stabilizing effect that tends to decrease the charge accumulation. If the relaxation of σ is sufficiently slow, this leads to a nonzero Hopf frequency, similar as in other convection systems with a stabilizing diffusion effect, such as convection in binary mixtures.

Results of a weakly nonlinear analysis of the WEM, using just a few particular modes, have been reported in [15,16]. They provided the first quantitative confirmation of the WEM at the linear level, in good agreement with some experiments [14], but still more accurate numerical computations as well as computations for other parameters and other types of instabilities are necessary to test the validity of the WEM. The patterns in the nematic I52, for instance, are dominated by oblique rolls [12], and checking if the WEM predicts oblique travelling waves is crucial for understanding the complex dynamics resulting from their interactions, observed in experiments, like spatiotemporal chaos at onset [5,8] and localized states known as worms [6].

In this paper we present a systematic bifurcation analysis of the WEM equations, when the primary instability is a Hopf bifurcation to oblique travelling rolls. We consider the limit of zero charge relaxation time and a constant external electric field. The methods we develop here can be applied to general two-dimensional extended anisotropic systems with translational and reflectional symmetries, as is the WEM. Since in such systems the minima on the neutral stability surfaces are isolated [17], they admit a unique reduced description through Ginzburg–Landau type amplitude equations at the onset, whose form is mainly determined by the symmetries of the governing PDEs and the type of instability (see [17–19]). In particular, in the case of a Hopf bifurcation with oblique travelling rolls, the reflection symmetries imply that the dynamics is governed by interactions of waves travelling in four directions.

We use the globally coupled system of four complex Ginzburg–Landau equations, derived in [17], to study the evolution of travelling wave envelopes arising in a weakly nonlinear analysis of the WEM equations. The modulational instability of pure travelling wave solutions has been studied and classified through Eckhaus stability boundaries in [25], for general parameters of the Ginzburg–Landau system. In [20] spatiotemporal complex dynamics, referred to as *zigzag chaos*, has been identified for a special set of parameters. The first comprehensive bifurcation analysis of the WEM, demonstrating the existence of a primary Hopf instability involving four oblique rolls, has been pursued in [26]; the parameters varied have been the elastic constants, with the other parameters matched to estimated values of the nematics I52 and MBBA. Here we extend the analysis of [26] by studying variations of the recombination and

mobility parameters, which are WEM specific (not present in the SM) and inaccessible experimentally. Furthermore, in order to study predicted electroconvective patterns above threshold for I52, we complement the bifurcation analysis with numerical simulations of the Ginzburg–Landau system and its normal form. We are particularly interested in identifying parameter regimes for which the Ginzburg–Landau analysis predicts different stable waves above onset, and comparing these predictions with the patterns observed experimentally.

Our analysis extends the work of [16] to include counterpropagating travelling waves too, hence the possibility of existence of other patterns like the alternating waves, observed experimentally in [8] and identified by us to have significant contribution to the structure and dynamics of the zigzag spatiotemporal chaos [20]. We find normal rolls, different types of oblique travelling wave patterns as well as more complex spatiotemporal structures, including quasi-periodic patterns, heteroclinic cycles, a period doubling cascade towards a chaotic attractor, and spatiotemporal chaos dominated by holes, dislocations, phase slips and grain boundaries.

The paper is organized as follows. In Section 2 we introduce the basic model equations for the rescaled WEM. In Section 3 we discuss the linear stability analysis of the WEM. The minimum of the neutral stability surface is calculated numerically, by means of a Nelder–Mead method combined with an augmented system for detecting Hopf bifurcation. In Section 4 we introduce the Ginzburg–Landau formalism for two-dimensional anisotropic extended systems and give a brief derivation of the four globally coupled complex Ginzburg–Landau equations we use in the weakly nonlinear analysis of the WEM. In Section 5 we present the results of the bifurcation analysis of the weak electrolyte model, for values of the parameters corresponding to the measured values of the nematic I52. The stability of the predicted convective patterns beyond threshold is classified in the context of the ODE normal form to which the Ginzburg–Landau system reduces when spatial variations are ignored. In addition, the Eckhaus stability for travelling waves occurring in the stability diagrams is investigated using the methods of [25]. In regions in the parameters space where no stable basic solutions are predicted, we study numerically the normal form dynamics, as well as the spatiotemporal dynamics of the Ginzburg–Landau system of amplitude equations. Section 6 concludes with discussions and an outlook of further work.

2. The weak electrolyte model for electroconvection in nematic liquid crystals

Nematic liquid crystals are charge carrying fluids with long range, uniaxial orientation and molecular alignment, giving rise to anisotropic macroscopic properties. Local orientation of molecules is macroscopically described by the director field $\mathbf{n}$. The external electric field causes the instability of the equilibrium state, leading to electroconvective motion. The standard experimental situation is a layer of nematic liquid crystals sandwiched between two horizontal plates with planar alignment of the director. An applied voltage (typically low frequency ac) induces an external alternating electric field in the z-direction. Usually the aspect ratios are large and can be idealized to be infinite, thus the layer is considered to be infinitely extended in the (x, y)-directions. In the approximation of a linear recombination term and zero diffusivity at the ions, the evolution equations of the WEM in dimensionless units [15,16] consist of an equation for the local conductivity σ resulting from the ion dissociation–recombination dynamics

$$(\partial_t + \mathbf{v}\cdot\nabla)\sigma = -\alpha^2\pi^2\nabla\cdot(\boldsymbol{\mu}\mathbf{E}\rho) - \frac{r}{2}(\sigma^2 - 1 - P_1\pi^2\alpha\rho^2), \tag{1}$$

the equation for the director $\mathbf{n}$ ($|\mathbf{n}| = 1$)

$$(\partial_t + \mathbf{v}\cdot\nabla)\mathbf{n} = \omega\times\mathbf{n} + \mathbf{d}(\lambda\mathbf{A}\mathbf{n} - \mathbf{h}), \tag{2}$$

the conservation of charge governing the evolution of the internally generated electric potential Φ

$$P_1(\partial_t + \mathbf{v}\cdot\nabla)\rho = -\nabla\cdot(\boldsymbol{\mu}\mathbf{E}\sigma), \tag{3}$$

together with Poisson's law for the electric charge density ρ

$$\rho = \nabla\cdot(\boldsymbol{\epsilon}\mathbf{E}), \tag{4}$$

and the generalized Navier–Stokes equations for velocity $\mathbf{v}$ and pressure p in anisotropic fluids

$$P_2(\partial_t + \mathbf{v}\cdot\nabla)\mathbf{v} = -\nabla p - \nabla\cdot(\mathbf{T} + \Pi) + \pi^2\rho\mathbf{E}, \tag{5}$$

$$\nabla\cdot\mathbf{v} = 0. \tag{6}$$

We use the scaling introduced in [15] in which lengths, time, orientational elasticities, viscosities, dielectric permittivities, and voltages are measured in units of d/π (d: distance between the plates), director relaxation time τ_d, splay deformation constant K_1, $\gamma_1 = \tilde{\alpha}_3 - \tilde{\alpha}_2$, $\epsilon_0\epsilon_\perp$, and V_c, respectively, where

$$\tau_d = \frac{\gamma_1 d^2}{K_1 \pi^2}, \qquad V_c = \sqrt{\frac{K_1 \pi^2}{\epsilon_0 \epsilon_\perp}},$$

$\epsilon_0\epsilon_\perp$ is the dielectric permittivity and $\tilde{\alpha}_j$ ($1 \leqslant j \leqslant 6$) are the Leslie coefficients. The Prandtl-type number P_1 is the ratio of the charge relaxation time τ_q and the director relaxation time, $P_1 = \tau_q/\tau_d$, where $\tau_q = \epsilon_0\epsilon_\perp/\sigma_\perp$ and $\sigma_\perp$ is the electric conductivity; the Prandtl-type number P_2 represents the ratio of the viscous (momentum diffusion) time and τ_d, $P_2 = \tau_{\text{visc}}/\tau_d$, where $\tau_{\text{visc}} = d^2\rho_m/\gamma_1$, ρ_m being the mass density. Conductivities are measured in units of the equilibrium conductivity $\sigma_{\text{eq}} = (\mu^+ + \mu^-)en_0$, defined in terms of the mobilities $\mu^\pm$, the elementary charge e and the equilibrium concentration n_0 of the ions. The WEM parameters α (the mobility parameter) and r (the recombination parameter) are [15]

$$\alpha = \sqrt{\frac{\mu^+\mu^-\gamma_1\pi^2}{\sigma_{\text{eq}} d^2}}, \qquad r = \frac{\tau_d}{\tau_{\text{rec}}},$$

where $\tau_{\text{rec}} = (2k_r n_0)^{-1}$ is the recombination time, k_r being the recombination constant. Both of these parameters are also Prandtl-type time scale ratios.

In the above equations $\mathbf{E} = (\sqrt{2R}/\pi)\cos(\omega_0 t)\mathbf{e}_3 - \nabla\Phi$ represents the electric field, $\omega = 1/2(\nabla \times \mathbf{v})$ is the vorticity and $\mathbf{A}$, with components $A_{ij} = \frac{1}{2}(v_{i,j} + v_{j,i})$, is the strain tensor. The molecular field

$$\mathbf{h} = \left(\frac{\partial f}{\partial \mathbf{n}} - \nabla \cdot \frac{\partial f}{\partial \nabla \mathbf{n}}\right) - \varepsilon_a \pi^2 (\mathbf{n} \cdot \mathbf{E})\mathbf{E},$$

is derived from the elastic energy density,

$$2f = K_1(\nabla \cdot \mathbf{n})^2 + K_2\big[\mathbf{n} \cdot (\nabla \times \mathbf{n})\big]^2 + K_3\big[\mathbf{n} \times (\nabla \times \mathbf{n})\big]^2,$$

due to splay (K_1), twist (K_2), and bend (K_3) deformations; in our scaling the splay deformation coefficient K_1 is normalized to unity. The tensors $\boldsymbol{\mu}$, $\boldsymbol{\epsilon}$, $\mathbf{d}$, $\boldsymbol{\Pi}$, $\mathbf{T}$ are the scaled mobility, dielectric, projection, Ericksen stress and viscous stress tensors, respectively, with components

$$\mu_{ij} = \delta_{ij} + \sigma_a n_i n_j, \quad \epsilon_{ij} = \delta_{ij} + \epsilon_a n_i n_j, \quad d_{ij} = \delta_{ij} - n_i n_j, \quad \Pi_{ij} = \frac{\partial f}{\partial n_{k,j}} n_{k,i},$$
$$-T_{ij} = \alpha_1 n_i n_j n_k n_l A_{kl} + \alpha_2 n_j N_i + \alpha_3 n_i N_j + \alpha_4 A_{ij} + \alpha_5 n_j n_k A_{ki} + \alpha_6 n_i n_k A_{kj},$$

where $\mathbf{n} = (n_1, n_2, n_3)$, $\mathbf{N} = \mathbf{d}(\lambda\mathbf{A}\mathbf{n} - \mathbf{h})$, ε_a and σ_a are the anisotropies of the dielectric permittivity and the electric conductivity at the equilibrium, respectively. The scaled Leslie coefficients $\alpha_1, \ldots, \alpha_6$ ($\alpha_j = \tilde{\alpha}_j/\gamma_1$) and the Onsager coefficient λ in (2) satisfy the Onsager relations $\alpha_1 + \alpha_3 = \alpha_6 - \alpha_5$, $\alpha_3 - \alpha_2 = 1$, $\lambda = \alpha_5 + \alpha_6$, and can be expressed in terms of the four independent parameters (Miesowicz coefficients) $\eta_0, \eta_1, \eta_2, \eta_3$, where $\eta_0 = \alpha_1 + \alpha_4 + \alpha_5 + \alpha_6$, $\eta_1 = (-\alpha_2 + \alpha_4 + \alpha_5)/2$, $\eta_2 = (\alpha_3 + \alpha_4 + \alpha_6)/2$, $\eta_3 = \alpha_4/2$, as

$$\lambda = \eta_1 - \eta_2, \quad \alpha_1 = \eta_0 - 2\eta_1 - 2\eta_2 + 2\eta_3 + 1, \quad \alpha_2 = -(1+\lambda)/2, \quad \alpha_3 = (1-\lambda)/2,$$
$$\alpha_4 = 2\eta_3, \quad \alpha_5 = 2\eta_1 - 2\eta_3 - (1+\lambda)/2, \quad \alpha_6 = 2\eta_2 - 2\eta_3 - (1-\lambda)/2.$$

The units are normalized such that the height of the nematic layer is π. Using the common planar alignment, the coordinate system is chosen such that $\mathbf{n} = (1, 0, 0)$ at the upper and lower plates located at $z = \pm\pi/2$. The 'rigid' blocking electrodes (i.e. no transfer of any charge through electrodes) boundary conditions on top and bottom of the layer,

$$\frac{\partial \sigma}{\partial z}, n_2, n_3, \phi, \mathbf{v} = 0 \quad \text{at } z = \pm\pi/2, \tag{7}$$

are deduced from the ideal conducting plates condition, rigid anchoring for the director, and finite viscosity.

The system (1)–(7) has reflectional

$$(x, n_2, n_3, v_1) \to (-x, -n_2, -n_3, -v_1),$$
$$(y, n_2, v_2) \to (-y, -n_2, -v_2),$$
$$(z, n_3, v_3, \Phi) \to (-z, -n_3, -v_3, -\Phi)$$

and translational

$$(x, y) \to (x + \xi, y + \eta)$$

symmetries (fields that preserve their signs are suppressed) due to the assumption of an infinitely extended layer in x and y, but there are no rotational symmetries due to the anisotropy of the system. The resulting symmetry group is $E_1 \times E_1 \times Z_2$ and the compactified symmetry group, in case of periodic boundary conditions in (x, y), is $O(2) \times O(2) \times Z_2$.

The system (1)–(6) depends on the main parameters driving the instability R and ω_0 (amplitude and frequency of the external electric field), four Prandtl-type time scale ratios P_1, P_2, α and r, the anisotropy coefficients ε_a and σ_a, and the material parameters $K_2, K_3, \eta_0, \eta_1, \eta_2, \eta_3$. Typically the Prandtl numbers P_1, P_2 are very small compared to the other parameters, at least in the conduction range, thus one can take the limit $P_2 = 0$ (zero viscous relaxation time) and $P_1 = 0$ (zero charge relaxation time) [15]. In this limit the WEM equations (1)–(6) split into the evolution equations for the variables σ and $\mathbf{n}$

$$(\partial_t + \mathbf{v} \cdot \nabla)\sigma = -\alpha^2 \pi^2 \nabla \cdot (\boldsymbol{\mu} \mathbf{E} \rho) - \frac{r}{2}(\sigma^2 - 1), \tag{8}$$
$$(\partial_t + \mathbf{v} \cdot \nabla)\mathbf{n} = \omega \times \mathbf{n} + \mathbf{d}(\lambda \mathbf{A}\mathbf{n} - \mathbf{h}), \tag{9}$$

and the equations for $\mathbf{v}$, p and Φ

$$-\nabla p - \nabla \cdot (\mathbf{T} + \boldsymbol{\Pi}) + \pi^2 \rho \mathbf{E} = 0, \qquad \nabla \cdot \mathbf{v} = 0, \tag{10}$$
$$-\nabla \cdot (\boldsymbol{\mu} \mathbf{E} \sigma) = 0, \tag{11}$$

with

$$\rho = \nabla \cdot (\boldsymbol{\epsilon} \mathbf{E}), \qquad \mathbf{E} = (\sqrt{2R}/\pi)\cos(\omega_0 t)\mathbf{e}_3 - \nabla \Phi. \tag{12}$$

and the boundary conditions (7).

Eqs. (8)–(11) are extremely complicated for a full 3D simulation, therefore a bifurcation study near onset is particularly useful. We present, in the next sections, a systematic linear stability analysis of the WEM equations (8)–(11), demonstrating the existence of primary instabilities of Hopf type involving two as well as four oblique rolls, thus breaking the reflection symmetry.

3. Linear stability analysis

We consider in this paper the WEM equations in the limit of zero viscous and charge relaxation time (8)–(11) with the boundary conditions (7) and we assume a constant external electric field in the z-direction ($\omega_0 = 0$), therefore $\mathbf{E} = (\sqrt{2R}/\pi)\mathbf{e}_3 - \nabla \Phi$. In order to determine the threshold R_c and the critical wave number $\mathbf{q}_c = (p_c, q_c)$ we investigate the linearized problem around the basic nonconvective state, given by $\sigma = 1$, $\mathbf{v} = 0$, $\Phi = 0$, $\mathbf{n} = (1, 0, 0)$, p = *const* [15]. In this limit Eqs. (8) and (9) do not depend on the time derivatives of $\mathbf{v}$ and Φ, respectively, hence these variables play the role of 'slaved variables', leading to a dynamical system for the three 'master' scalar fields (σ, n_2, n_3).

The stability of the basic state is governed by linearized equations for perturbational fields $\delta\sigma$, δn_2, δn_3, $\delta\phi$, δv_j, $j = 1, \ldots, 3$, δp. Due to the translation invariance w.r.t. (x, y), the perturbational fields can be represented by horizontal Fourier modes,

$$(\delta\sigma, \delta n_2, \delta n_3, \delta\phi, \delta v_j, \delta \mathrm{p}) = e^{i(px+qy)}(\Sigma, N_2, N_3, \Phi, V_j, \mathrm{P}),$$

where Σ, N_2 etc. depend on (t, z, p, q) and the parameters. The velocities V_j are represented by poloidal and toroidal stream functions F and G leaving us with a system of linear equations for $(\Sigma, N_2, N_3, \Phi, F, G)$. With the notations $D = (\Sigma, N_2, N_3)$, $S = (\Phi, F, G)$ the linearized WEM equations can be written symbolically as

$$D_t = \mathcal{L}_D(D, S) \equiv \mathcal{L}_{DD}(p, q, R)D + \mathcal{L}_{DS}(p, q, R)S, \tag{13}$$

$$0 = \mathcal{L}_S(D, S) \equiv \mathcal{L}_{SD}(p, q, R)D + \mathcal{L}_{SS}(p, q, R)S, \tag{14}$$

where $\mathcal{L}_D = (\mathcal{L}_\Sigma, \mathcal{L}_{N_2}, \mathcal{L}_{N_3})$, $\mathcal{L}_S = (\mathcal{L}_\Phi, \mathcal{L}_F, \mathcal{L}_G)$ are linear differential operators w.r.t. z. The explicit form of these equations is summarized in Appendix A (Eqs. (A.1)–(A.4) and (A.5)–(A.7)). The boundary conditions (7) in the new variables read as

$$\frac{\partial \Sigma}{\partial z} = N_2 = N_3 = 0, \quad F = \frac{\partial F}{\partial z} = G = 0 \quad \text{at} \quad z = \pm\pi/2. \tag{15}$$

Formally, (13)–(14) form a linear dynamical system for D,

$$D_t = L(D|p, q, R), \tag{16}$$

obtained by solving (14) for $S(D|p, q, R) = -\mathcal{L}_{SS}^{-1}\mathcal{L}_{SD}D$ and substituting this into (13). Since the solution $S(D|p, q, R)$ with the given boundary conditions is represented by an integral operator, $L = (\mathcal{L}_{DD} - \mathcal{L}_{DS}\mathcal{L}_{SS}^{-1}\mathcal{L}_{SD})$ is an integro-differential operator with respect to z. The solution of (14) is facilitated by the fact that the Φ-component does not depend on the velocity.

For given material and system parameters the complex growth rate depends on R, p and q. The transition to instability occurs at a minimum $R_c = R(p_c, q_c)$ on the neutral stability surface (NSS) $R(p, q)$, on which the basic state is marginally stable against plane wave perturbations with wave numbers (p, q). The NSS is derived from $\mu_r(p, q, R) = 0$, where $\mu(p, q, R) = \mu_r(p, q, R) + i\omega(p, q, R)$ is the critical eigenvalue of the linearized system (16). The threshold values (p_c, q_c) and $\omega_c = \omega(p_c, q_c, R_c)$ are referred to as the critical wave numbers and frequency, respectively. Usually there is a stationary NSS on which $\omega = 0$ and an oscillatory NSS on which $\omega \neq 0$. The transition to instability occurs on the NSS with the lower minimum and gives rise either to a stationary bifurcation ($\omega_c = 0$) or a Hopf bifurcation ($\omega_c \neq 0$). Since the system is reflection invariant about both the x- and y-axes and has no rotational symmetry, the p- and q-axes are symmetry axes of the neutral stability surface.

Due to the anisotropy the minima on the NSS are isolated. There are three qualitatively distinct scenarios for the location of the minima: (a) the critical wave vector is zero, (b) there are two critical wave vectors $(\pm p_c, 0)$ on a symmetry axis (normal rolls), and (c) there are four critical wave vectors $(\pm p_c, \pm q_c)$ off both symmetry axes (oblique rolls).

A previous linear stability study, done in [15,16], was based on a few mode approximation in which the z dependence of the velocity was approximated by two Chandrasekhar modes, only three Fourier modes were taken into account w.r.t. t, and only three vertical modes were used to represent the dynamical variables (σ, n_2, n_3). To perform a systematic Galerkin approximation of L w.r.t. D, we use in our analysis natural, sine- and cosine vertical modes adapted to the boundary conditions. Due to the z-reflectional symmetry L has odd and even invariant subspaces spanned by modes of the form $D_m = (a_1 \sin(2m-1)z, a_2 \sin 2mz, a_3 \cos(2m-1)z)$, $m \geqslant 1$ odd, and $E_m = (a_1 \cos 2mz,\ a_2 \cos(2m+1)z, a_3 \sin 2mz)$, $m \geqslant 0$ even, respectively. For the parameter range considered here the instability occurs in the odd subspace. In this subspace L is represented by an infinite matrix $\mathcal{M}$ composed of 3×3 blocks $M(m, n)$ defined by

$$M_{ij}(m, n) = \frac{2}{\pi} \int_{-\pi/2}^{\pi/2} L(D_{mi}) \cdot D_{nj}\, dz, \quad 1 \leqslant i, j, \leqslant 3, \tag{17}$$

where D_{mi} is the D_m mode with $a_j = \delta_{ij}$. To find these matrices, for any mode D_m we compute the exact solution $S_m = S(D_m|p, q, R)$ of the nonhomogeneous equations (14) subject to the boundary conditions and then evaluate the resulting integral (17) analytically. The solution of the Φ-equation is straightforward and preserves the chosen modes. In contrast, the solution of the F and G-equations involves hyperbolic functions leading to a transcendental dependence of the M_{ij} on (p, q).

To compute the critical data (p_c, q_c, R_c) numerically we used a $3N \times 3N$ truncation of $\mathcal{M}$ by restricting (m, n) to $1 \leqslant m, n \leqslant N$. We move progressively to higher values of N, using the previously computed values as starting values for the numerical search. The task of determining the local form of the critical eigenvalue near the minimum of the NSS involves a three parameter Hopf computation. For $N = 1$, the analytically derived equations for an imaginary eigenvalue of a 3×3 matrix and for a minimum of R are solved numerically and the results are used as a starting value

for the calculations with $N > 1$, for which the NSS is computed with Werner's augmented system [21] and minimized using a Nelder–Mead method [22]. Numerical convergence with an accuracy up to five significant figures was usually observed for $N \geqslant 9$. The bifurcation diagrams for values of the parameters for the nematic liquid crystal I52, as well as the results of the weakly nonlinear analysis of basic wave patterns for these parameters are presented in Section 5.

4. Ginzburg–Landau analysis of the WEM

The weak electrolyte model is a particular case of an axially anisotropic, dissipative systems with two extended dimensions (x, y). In such systems, the axial anisotropy induces reflection and translation invariance in both extended directions, thus the underlying symmetry group is $E(1) \times E(1)$ which compactifies to $O(2) \times O(2)$ if periodic boundary conditions are imposed. In what follows we will derive the Ginzburg–Landau system of equations for two-dimensional anisotropic systems in the case of four minima of the neutral stability surface and we will use it to analyze the instabilities in the WEM.

4.1. Globally coupled Ginzburg–Landau equations

Since the case when $p_c = 0$ does not occur in experiments with planar alignment, there are two remaining types of Hopf bifurcation: the normal rolls, with $q_c = 0$, and the oblique rolls with $q_c \neq 0$. In this work we focus on the last case, with four minima of the neutral stability surface, and hence four critical wave numbers $(\pm p_c, \pm q_c)$. These wave numbers define two oblique ('zig' and 'zag') directions for two pairs of counterpropagating travelling waves of the linearized equations at onset. The solution of the WEM (8)–(11) slightly above R_c is represented by a superposition of two pairs of waves in the form

$$\begin{aligned}\mathbf{u}(t, x, y, z) = \big(&\mathcal{A}_1 e^{i(p_c x + q_c y)}\mathbf{U}_1(z) + \mathcal{A}_2 e^{i(-p_c x + q_c y)}\mathbf{U}_2(z) + \mathcal{A}_3 e^{i(-p_c x - q_c y)}\mathbf{U}_3(z)\\ &+ \mathcal{A}_4 e^{i(p_c x - q_c y)}\mathbf{U}_4(z)\big)e^{i\omega_c t} + \text{cc} + \text{h.o.t.},\end{aligned} \tag{18}$$

(cc = complex conjugate) where the $\mathcal{A}_j$, $j = 1, \ldots, 4$, are small, slowly varying envelopes, $\mathbf{U}_j(z)$ are the (symmetry related) vertical critical modes and h.o.t. refers to terms of higher order in $R - R_c$ and the $\mathcal{A}_j$ and their derivatives.

By means of a formal expansion in the $\mathcal{A}_j$ and their derivatives, as well as symmetry considerations, one can derive a system of modulation equations for the envelopes. The equation for $\mathcal{A}_1$ reads,

$$\mathcal{A}_{1t} + v_x \mathcal{A}_{1x} + v_y \mathcal{A}_{1y} = \left[a_0(R - R_c) + \widetilde{\mathcal{D}}(\partial_x, \partial_y) + \sum_{j=1}^{4} a_j |\mathcal{A}_j|^2\right]\mathcal{A}_1 + a_5 \mathcal{A}_2 \bar{\mathcal{A}}_3 \mathcal{A}_4 + \text{h.o.t.}, \tag{19}$$

where $(v_x, v_y) = \nabla\omega|_c$ are the two critical group velocities, $a_0, a_1, \ldots, a_5$ are complex coefficients, and

$$\mathcal{D}(\partial_x, \partial_y) = d_{20}\partial_x^2 + 2d_{11}\partial_x\partial_y + d_{02}\partial_y^2$$

is a complex second order differential operator with elliptic real part. The linear coefficients (v_x, v_y, a_0, and coefficients of $\mathcal{D}$) in (19) are determined by the first and second order expansion coefficients of the critical eigenvalue μ about criticality, and the nonlinear coefficients a_j, $1 \leqslant j \leqslant 5$, are determined by solving a sequence of nonhomogeneous linear problems derived from the quadratic and cubic terms of the WEM. The h.o.t. in (19) refers to higher order terms which do not contribute at leading order when (19) is rescaled and expanded in powers of $\varepsilon = \sqrt{R - R_c}$. The equations for $\mathcal{A}_2, \mathcal{A}_3, \mathcal{A}_4$ follow from (19) through appropriate reflection operations.

The system (19) is still in unscaled form. In the generic case in which v_x, v_y are of order 1, one has to resort to four slow wave variables $\xi_\pm = \varepsilon(x \pm v_x t)$, $\eta_\pm = \varepsilon(y \pm v_y t)$, adapted to the first order wave operator on the left-hand side of (19). It can be shown [17] that a consistent expansion $\mathcal{A}_j = \varepsilon A_j + \mathrm{O}(\varepsilon^2)$ requires that A_1, A_2, A_3, A_4 depend on $T = \epsilon^2 t$ and (ξ_+, η_+), (ξ_-, η_+), (ξ_-, η_-), (ξ_+, η_-), respectively, and that the A_j satisfy a system of four globally coupled complex Ginzburg–Landau equations (GCCGLE). The equation for A_1 is given by

$$\begin{aligned}A_{1T} = \Big\{&a_0 + \mathcal{D}(\partial_{\xi_+}, \partial_{\eta_+}) + a_1|A_1|^2 + a_2\big\langle\big|A_2(s, \eta_+)\big|^2\big\rangle + a_3\big\langle\big|A_3(\xi_+ + s, \eta_+ + s)\big|^2\big\rangle\\ &+ a_4\big\langle\big|A_4(\xi_+, s)\big|^2\big\rangle\Big\}A_1 + a_5\big\langle A_2(s + \xi_+, \eta_+)\bar{A}_3(\xi_+ + s, \eta_+ + s)A_4(\xi_+, \eta_+ + s)\big\rangle,\end{aligned} \tag{20}$$

where the brackets denote averages over s. The equations for A_2, A_3, A_4 follow from (20) through the reflection operations [17]

$$R_x : (A_1, A_2, A_3, A_4, x, y) \to (A_2, A_1, A_4, A_3, -x, y),$$
$$R_y : (A_1, A_2, A_3, A_4, x, y) \to (A_4, A_3, A_2, A_1, x, -y),$$

and $R_x R_y$, so that the full system of GCCGLE has two reflection symmetries. In addition, it has the normal form phase shift symmetry $A_j \to e^{i\varphi} A_j$ resulting from the temporal translation invariance of the underlying physical PDE-system, and two other phase shift symmetries,

$$(A_1, A_2, A_3, A_4) \to (e^{i\varphi_1+i\varphi_2} A_1, e^{-i\varphi_1+i\varphi_2} A_2, e^{-i\varphi_1-i\varphi_2} A_3, e^{i\varphi_1-i\varphi_2} A_4),$$

resulting from the translation invariance in the x- and y-directions. The envelopes (A_1, A_3) and (A_2, A_4) modulate counterpropagating travelling waves in the directions $\pm(p_c, q_c)$ and $\pm(-p_c, q_c)$, respectively. Accordingly we refer to (A_1, A_3) as "zig"-amplitudes and to (A_2, A_4) as "zag"-amplitudes.

The computation of the nonlinear coefficients a_j in the globally coupled Ginzburg–Landau equations (20), (21) proceeds by numerically evaluating their analytical representation in terms of the bilinear and cubic terms of the WEM equations (8)–(11) with an adjoint critical mode. This involves solving a hierarchy of nonhomogeneous linear equations, where at each stage the S-equations (14) are inverted numerically using the analytically derived Green's matrix of the S-part of L_S. We use the same Galerkin expansion for D as in the linear computations.

We write formally the third order expansion of the full nonlinear equations for the "dynamical variables" $D = (\sigma, n_2, n_3)$ at $R = R_c$ as

$$D_t = F\big(D, S(D)\big) = \mathcal{L}D + \mathcal{B}[D, D] + \mathcal{C}[D, D, D] + \cdots,$$

where $\mathcal{L}$ is a linear operator, and $\mathcal{B}$ and $\mathcal{C}$ are symmetric bilinear and trilinear operators, respectively. With the notation $\mathbf{k} = (p, q)$, $\mathbf{x} = (x, y)$, and $\mathbf{kx} = px + qy$, the Fourier representation of these operators can be written in the form

$$\mathcal{L}[e^{i\mathbf{kx}} D] = e^{i\mathbf{kx}} L(\mathbf{k})[D],$$
$$\mathcal{B}[e^{i\mathbf{k}_1\mathbf{x}} D_1, e^{i\mathbf{k}_2\mathbf{x}} D_2] = e^{i(\mathbf{k}_1+\mathbf{k}_2)\mathbf{x}} B(\mathbf{k}_1, \mathbf{k}_2)[D_1, D_2],$$
$$\mathcal{C}[e^{i\mathbf{k}_1\mathbf{x}} D_1, e^{i\mathbf{k}_2\mathbf{x}} D_2, e^{i\mathbf{k}_3\mathbf{x}} D_3] = e^{i(\mathbf{k}_1+\mathbf{k}_2+\mathbf{k}_3)\mathbf{x}} C(\mathbf{k}_1, \mathbf{k}_2, \mathbf{k}_3)[D_1, D_2, D_3],$$

with linear, bilinear and trilinear operators $L(\mathbf{k})$, $B(\mathbf{k}_1, \mathbf{k}_2)$, and $C(\mathbf{k}_1, \mathbf{k}_2, \mathbf{k}_3)$ that depend on the wave numbers and act on vertical functions $D(z)$, $D_j(z)$. If we let $D_c(z)$ be the vertical critical mode (the (σ, n_2, n_3)-components of $\mathbf{U}_1(z)$ in (18)), i.e. $L(\mathbf{k}_c)[D_c] = i\omega_c D_c$ with $\mathbf{k}_c = (p_c, q_c)$, the first nonlinear coefficient a_1 is given by

$$a_1 = \big\langle D_c^*, D_1^{(b)} + D_1^{(c)} \big\rangle,$$

where $\langle D, D' \rangle$ denotes the L_2-inner product of vertical functions $D(z)$, $D'(z)$, $D_c^*(z)$ is the adjoint critical mode, and

$$D_1^{(b)} = 2B(2\mathbf{k}_c, -\mathbf{k}_c)[D_{11}, \overline{D}_c] + 2B(\mathbf{0}, \mathbf{k}_c)[D_{10}, \overline{D}_c],$$
$$D_1^{(c)} = 3C(\mathbf{k}_c, \mathbf{k}_c, -\mathbf{k}_c)[D_c, D_c, \overline{D}_c],$$

with D_{11}, D_{10} given by the solutions of

$$L(2\mathbf{k}_c)[D_{11}] - 2i\omega_c D_{11} = -B(\mathbf{k}_c, \mathbf{k}_c)[D_c, D_c],$$
$$L(0)[D_{10}] = -2B(\mathbf{k}_c, -\mathbf{k}_c)[D_c, \overline{D}_c].$$

The coefficients a_2–a_5 are given by similar expressions. In the numerical computations the vertical functions are represented by vectors using the same basis functions as in the linear computations.

The coefficients of the quadratic expansion of the neutral stability surface about its minimum, in terms of which the operator $\mathcal{D}$ in (20) is defined, and the critical group velocities are found by least squares fits of the numerically computed neutral stability surface near (p_c, q_c) to second degree polynomials.

4.2. Solutions of the globally coupled Ginzburg–Landau equations

The Ginzburg–Landau system can be viewed as an extension of an ODE normal form in the context of the equivariant bifurcation theory, derived by a center manifold reduction from the WEM under the restriction that the fields be periodic in (x, y). While normal forms of equivariant bifurcation theory lead to spatiotemporal patterns with a fixed spatial period, the GCCGLE allow to extend these patterns to families of varying periods and to study their modulational stability against periodic perturbations with other periods.

With $(2\pi/p_c \times 2\pi/q_c)$-periodicity in (x, y) imposed, a center manifold reduction and normal form transformation applied to the WEM leads to the normal form for a Hopf bifurcation with $O(2) \times O(2)$-symmetry. This normal form follows directly from the globally coupled system (20) when spatial variations are ignored, i.e. $A_j = A_j(T)$. The equation for A_1 is given by

$$\frac{dA_1}{dT} = \left(a_0 + \sum_{j=1}^{4} a_j |A_j|^2\right) A_1 + a_5 A_2 \bar{A}_3 A_4, \tag{21}$$

and the equations for A_2, A_3, A_4 follow by applying the permutations (2, 1, 4, 3), (3, 1, 4, 2), (4, 3, 2, 1) to the indices of the A_j in (21), representing the reflections $x \to -x$, $(x, y) \to (-x, -y)$ and $y \to -y$. The normal form (21) has been introduced and analyzed independently by Silber et al. [23] and Wegelin [24]. It has six basic solutions corresponding to six basic wave patterns shown by $\mathbf{u}(t, x, y, z)$ when represented by (18): travelling (TW) and standing (SW) waves, two types of travelling rectangles (TR_x and TR_y, travelling in the x and y direction, respectively), standing rectangles (SR), and alternating waves (AW), which alternate periodically between differently oriented standing waves. Each of these waves can occur with different orientations, for example, a TW can propagate in any of the four directions $(\pm p_c, \pm q_c)$, and their stability in the ODE setting can be classified in terms of the nonlinear coefficients a_j (see [17,23,24]). Up to three basic wave patterns can be simultaneously stable, there are eight four-dimensional invariant subspaces and in one of them we can find quasiperiodic solutions, and several heteroclinic cycles connecting different basic periodic solutions can occur as attractors in certain parameter regimes.

The basic periodic solutions of (21) that reside in two-dimensional fixed point subspaces induce wave solutions of the original system with critical wave numbers (p_c, q_c). The globally coupled system of complex Ginzburg–Landau equations (20) allows to extend these solutions to families of wave solutions with nearby critical wave numbers $(p_c + \varepsilon p, q_c + \varepsilon q)$. If a basic wave pattern appears stable as solution of (21), the Eckhaus stability boundary (*ESB*) for fixed $R > R_c$ is a closed curve in the (p, q) plane that separates modulationally stable (interior of *ESB*) and unstable solutions of the family. The analysis for all the six wave patterns is algebraically very complicated due to the fact that the *ESB* of a particular wave pattern depends on all six coefficients of the differential operator $\mathcal{D}$ as well as on certain combinations of the a_j. A detailed study of the *ESB* for travelling waves, based on the linearization of (20), has been pursued in [25].

In the next section we present the results of a normal form and a Ginzburg–Landau analysis of the WEM, predicting stable basic wave patterns as well as more complex spatiotemporal patterns above the onset of electroconvection.

5. Numerical computations for the WEM

The rescaled WEM equations depend on the bifurcation parameter R and ten dimensionless material parameters. Eight of these parameters occur already in the standard model SM and are usually known experimentally. The remaining two parameters, r and α, are specific for the WEM. In our parameter study we fix six SM-parameters to measured values of the nematic I52 [15,12], and vary r and α as well as the two SM parameters K_2 and K_3 (ratios of the twist and bend distortion coefficients to the splay distortion coefficient).

We first compute the critical data (p_c, q_c, R_c) and the critical group velocities through a linear stability analysis, then we proceed to the numerical computation of the linear and nonlinear coefficients of the GCCGLE (20) from the WEM equations (8)–(11) for various choices of the parameters [26]. The main goal is to demonstrate the presence of a primary Hopf-type instability for which the patterns of the linearized system are a superposition of four oblique travelling rolls with wave numbers $(\pm p_c, \pm q_c)$, and to analyze the stable patterns predicted by this instability above threshold. We always found $p_c \neq 0$, in agreement with the experiments.

We identify basic wave patterns occurring stable as solutions of (21), in different regions of the parameter space. Their stability is classified in terms of the coefficients $a_1, \ldots, a_5$. In regions where no stable basic solutions are

predicted, we complement our analysis with the numerical study of the normal form (21) dynamics and compare it with the numerical simulation of the spatiotemporal dynamics of the Ginzburg–Landau equations (20). We conclude with a discussion on the Eckhaus stability for the travelling waves identified in the stability diagrams. We summarize the results of this parameter study in the next subsections.

5.1. Stability diagrams

We first performed (r, α)-scans for three sets of values of K_2, K_3. The other SM-parameters have been fixed to their measured values at the temperature 45 °C as

$$\eta_0 = 0.8038, \quad \eta_1 = 0.8769, \quad \eta_2 = 0.0769, \quad \eta_3 = 0.1019, \quad \varepsilon_a = -0.0089, \quad \sigma_a = 0.38. \tag{22}$$

The chosen parameter sets for K_2, K_3 are (a) $K_2 = 0.6053$, $K_3 = 1.2105$, (b) $K_2 = 0.6875$, $K_3 = 1.25$, and (c) $K_2 = 0.875$, $K_3 = 1.25$. The values for the set (b) have been used in [15]; the values for (a) and (c) are nearby values, chosen to capture the changes in the stability diagrams when K_2, K_3 vary.

Fig. 1 summarizes the results in the form of stability diagrams in the (r, α)-plane for all three cases. In each case we have two separation curves C_1 and C_2 between three different regions of stability, labelled 'STEADY ROLLS', 'SUBCRITICAL WAVES', and 'STABLE WAVES', respectively.

Above the curve C_2 we find Hopf bifurcation with both p_c, q_c nonzero. Below this curve stationary instabilities (steady rolls) occur; this region has not been analyzed further. The boundary curve C_1 encloses the region (STABLE WAVES) in which the dynamics of (21) is bounded. In the adjacent region (SUBCRITICAL WAVES) at least one of the basic waves described in Section 4.2 bifurcates subcritically, causing a global instability for (21). The waves marked in this region are subcritical for (r, α) near the location of their names. Note that up to four different waves (*TW*, *SW*, *AW*, *SR*) can be subcritical simultaneously.

In the region enclosed by C_1 (STABLE WAVES) we identify stable solutions of (21) and mark the location where they occur by their names. We have found all basic waves described in Section 4.2 as well as small regions with the possibility of stable quasiperiodic solutions (*QP*) and structurally stable and attracting heteroclinic cycles. (*HC*). The stability of the basic waves is fully determined by the coefficients $a_1, \ldots, a_5$. In contrast, we can only check necessary conditions for the existence of heteroclinic cycles, but if they exist their stability is also fully determined by the nonlinear coefficients. The quasiperiodic solutions reside in certain four-dimensional fixed point subspaces. The normal form restricted to these subspaces coincides with a D_4-equivariant Hopf normal form, and so we can check the conditions given by Swift [27] for the possibility of a supercritical torus bifurcation. These conditions are only indicative of the existence of an attracting quasiperiodic orbit, and numerical simulations have to be performed to confirm it. The possibility of stable *QP*'s is found in all three scans, but an *HC*-region could only be identified in Fig. 1(c). This heteroclinic cycle connects TR_y, *AW*, and *SW*.

In all three scans we observe bistability regions, with either TR_x and TR_y, or *SR* and *SW*, or *AW* and *SW*, or TR_x and *SW* being simultaneously stable. In Fig. 1(b) we also see a bistability region with TR_x and possibly *QP* simultaneously stable, and in Fig. 1(c) a region with the possibility of *QP* and *HC* simultaneously stable. Results of numerical simulations in the latter region, showing a period doubling cascade towards a chaotic attractor for (21), and temporal as well as spatiotemporal chaos in (20), respectively, are presented in the next two subsections.

In Table 5 (Appendix B) we present typical linear critical data for the cases (a)–(c) represented in Fig. 1, computed for fixed $r = 0.02$ and α varying from 0.01 to 0.035. The table shows p_c, q_c, R_c together with the associated Hopf frequencies and the critical group velocities.

We have done the same calculations for the material parameters of I52 measured at the temperatures 30 °C, 50 °C and 60 °C. The resulting stability diagrams are qualitatively similar to Fig. 1, with the stable wave region enclosed by C_1 getting smaller/larger for decreasing/increasing temperature.

The first Ginzburg–Landau analysis of the WEM has been performed in [15,16] for different parameter ranges, including the parameter regime we used in our calculations for Fig. 1(b). Among the nonlinear coefficients, only the coefficients a_1 and a_2 have been computed in [15] and [16], respectively, and no analysis of the six basic wave solutions of (21) has been given. Our separation curve C_2 between the stationary and Hopf regimes coincides qualitatively with the same separation curve (denoted also C_2) in Fig. 6.4 of [15]. The quantitative differences are presumably due to the fact that in [15,16] (i) only five vertical modes have been used in the calculation, (ii) the computations are done for *ac*-frequency with small, but still nonzero external frequency, and (iii) r and α have been treated as perturbation

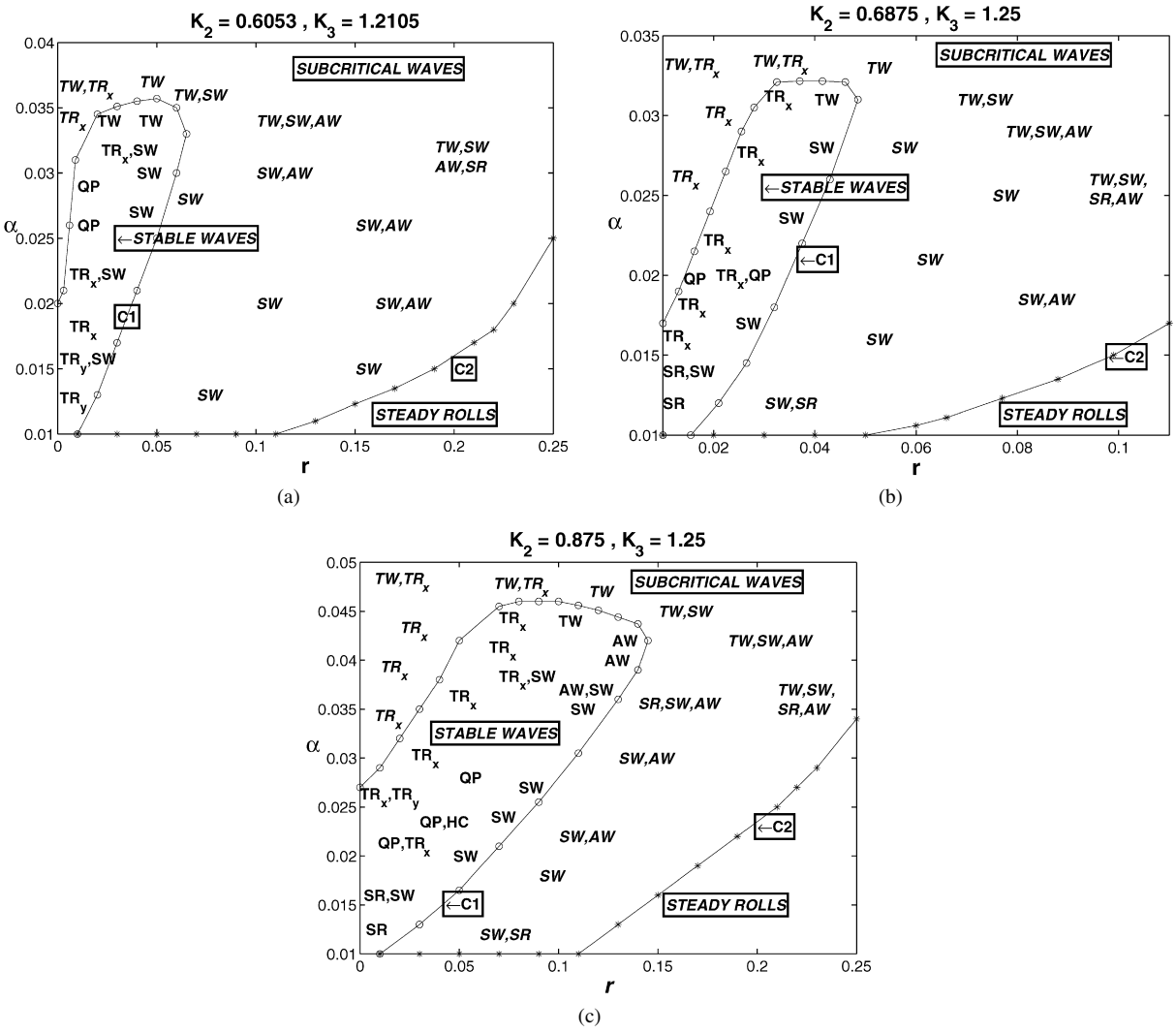

Fig. 1. Stability diagrams in the (r, α)-plane showing stable and subcritical waves predicted by (21), with coefficients calculated from the WEM for the parameters (22) (I52 at temperature 45 °C) and three sets of values for K_2, K_3: (a) $K_2 = 0.6053$, $K_3 = 1.2105$, (b) $K_2 = 0.6875$, $K_3 = 1.25$ (same as in [15]), (c) $K_2 = 0.875$, $K_3 = 1.25$.

Table 1
Parameter values of the WEM used in the computations for Fig. 2(a)–(d)

	η_0	η_1	η_2	η_3	ϵ_a	σ_a	r	α
(a)	0.7913	0.8707	0.0707	0.0957	-0.0162	0.26	0.0894	0.0386
(b)	0.8038	0.8769	0.0769	0.1019	-0.0089	0.38	0.0453	0.0196
(c)	0.8369	0.8935	0.0935	0.1185	-0.0015	0.45	0.0281	0.0113
(d)	0.8138	0.8669	0.0869	0.1019	-0.0089	0.38	0.0208	0.0210

parameters about the SM. Our region with stable waves is smaller than the corresponding region in [15]. This is due to the fact that our curve C_1 is determined by supercritical–subcritical transitions of the basic waves, which are not (except for *TW*) amenable when only one envelope is taken into account. The fact that in [15] the stationary bifurcation is subcritical near the curve C_2 is consistent with our finding that in the Hopf regime near C_2 at least one basic wave is subcritical, although we have not done nonlinear computations in the stationary regime.

To demonstrate the transition from oblique to normal travelling rolls, we next varied K_2, K_3 and kept the remaining parameters fixed at the values summarized in Table 1. The parameter sets (a), (b) and (c) in this table are calculated

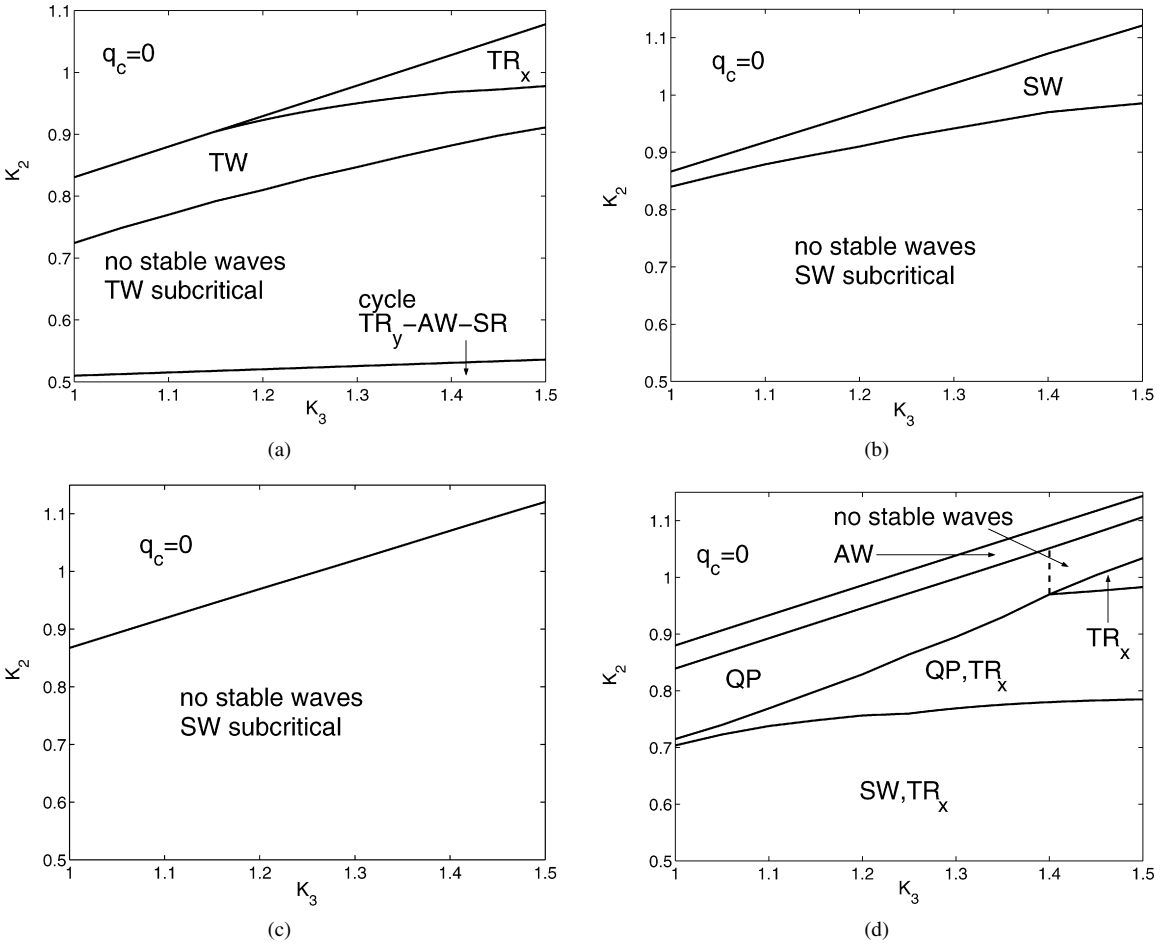

Fig. 2. Stability diagrams in the (K_3, K_2) plane. The parameter values of the WEM for cases (a)–(d) are listed in Table 1.

from measured and estimated values for I52 at 30 °C, 45 °C and 60 °C, respectively [15]. The values (d) in Table 1 are perturbations of (b). Fig. 2 summarizes the results again in the form of stability diagrams. In each diagram we observe a separation curve on which the pairs $(p_c, \pm q_c)$ and $(-p_c, \pm q_c)$ of the four minima of the neutral stability surface merge and degenerate in the q-direction, leaving only two minima at $(\pm p_c, 0)$ (normal travelling rolls) above that curve. The points on this curve are referred to as Lifschitz points. To the right of the (approximately vertical) dashed curve in Fig. 2(d) we find no stable waves, but also no subcritical waves, thus we can expect more complicated dynamics for (21), and presumably complex spatiotemporal behavior for (20).

5.2. Normal form dynamics

Here we report on a specific sequence of bifurcations observed in numerical simulations of (21) for values of the coefficients $a_0, \ldots, a_5$ calculated from the WEM. The overall bifurcation is a transition from a quasiperiodic attractor to a travelling rectangle via a cascade of period doubling bifurcations and a reverse cascade of period doubling. This scenario occurs for $r = 0.03$ and α varying from 0.024 to 0.026, with the other parameters fixed as in the calculations for Fig. 1(c).

In Fig. 3 we show four time series of the absolute values of the $A_j(T)$, $1 \leqslant j \leqslant 4$, for $\alpha = 0.024, 0.025, 0.02515$ and 0.0252. The values of the a_j resulting from these values of α and the initial conditions chosen for the simulations are summarized in Table 2 (a) and (b), respectively. Note that we use here a normalization and scaling of the A_j such that $a_{0r} = 1$ and $a_{1r} = -1$ in the supercritical case $a_{1r} < 0$.

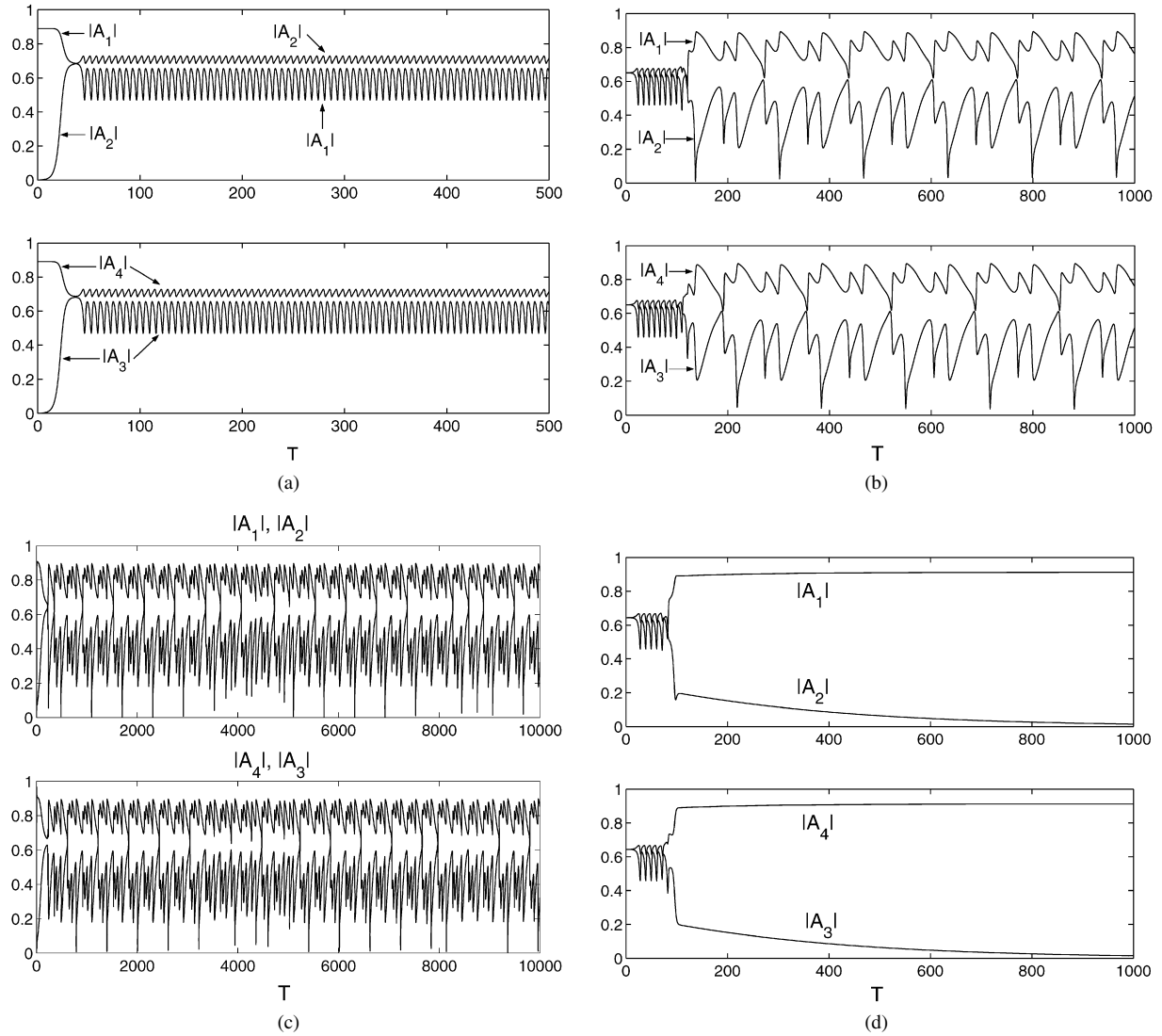

Fig. 3. Time series $|A_j(T)|$, $1 \leqslant j \leqslant 4$, obtained from numerical simulations of (21) for the coefficients summarized in Table 2(a), for (a) $\alpha = 0.024$, (b) $\alpha = 0.025$, (c) $\alpha = 0.02515$, and (d) $\alpha = 0.0252$. In (c) the upper time series in the two plots are for $|A_1|$, $|A_4|$, and the lower time series for $|A_2|$, $|A_3|$.

At $\alpha = 0.024$, the linear stability analysis predicts no stable waves, but the possibility of an attracting quasiperiodic solution QP_1 residing in the 4d fixed point subspace $(A_1, A_2, A_3, A_4) = (A, B, A, B)$. This prediction has been confirmed by numerical simulations for several initial conditions. In Fig. 3(a) we show the time series of the $|A_j(T)|$ for QP_1 resulting from a simulation with initial condition close to a travelling rectangle $(A, 0, 0, A)$, see Table 2(b).

Slightly above $\alpha = 0.024$ the QP_1 becomes unstable, and we observe attraction to another quasiperiodic solution QP_2 (not shown) in the 4d subspace (A, B, B, A). When α increases towards 0.025, QP_2 also becomes unstable. For this value of α the necessary conditions for the existence of an attracting heteroclinic cycle are satisfied, but we could not find this cycle in our simulations. Instead, we found an attracting orbit that is periodic in the absolute values (presumably also quasiperiodic in the full (A_1, A_2, A_3, A_4)-space) with a long period. The time series of this orbit is shown in Fig. 3(b). The choice of the initial condition (close to AW, which resides in the same 4d subspace as QP_1) leads first to QP_1 for a certain transient time before the attracting orbit with large period is approached – this is not the case for initial conditions close to TR_x. This attracting orbit does not reside in a 4d fixed point subspace and is not a structurally stable heteroclinic cycle (confirmed through numerical simulation up to $T = 5 \times 10^5$). The orbit

Table 2
(a): $a_0, a_1, \ldots, a_5$ calculated from the WEM for the four values of α in the first column, $r = 0.03$, and the other parameters as in the calculation for Fig. 1(c). (b): Initial conditions chosen for the simulations of (21) for the coefficients given in (a)

(a)	α	a_0	a_1	a_2	a_3	a_4	a_5
	0.024	1	−1	−0.8353	−0.4339	−0.2640	−0.3936
		$-0.0991i$	$-1.1504i$	$-0.5529i$	$+1.1877i$	$-3.1457i$	$-0.2751i$
	0.025	1	−1	−0.9390	−0.6869	−0.2148	−0.4777
		$-0.0917i$	$-1.1860i$	$-0.5540i$	$+1.3927i$	$-3.3309i$	$-0.2421i$
	0.02515	1	−1	−0.9501	−0.7135	−0.2097	−0.4867
		$-0.0909i$	$-1.1896i$	$-0.5541i$	$+1.4141i$	$-3.3502i$	$-0.2386i$
	0.0252	1	−1	−0.9613	−0.7405	−0.2047	−0.4958
		$-0.0902i$	$-1.1932i$	$-0.5542i$	$+1.4356i$	$-3.3696i$	$-0.2350i$

(b)	α	$A_1(0)$	$A_2(0)$	$A_3(0)$	$A_4(0)$
	0.024	0.8895	$0.0001i$	$0.001i$	0.8895
	0.025	0.6505	$0.0001 + 0.6505i$	0.6505	$0.001 + 0.6505i$
	0.02515	0.001	$0.0001 + 0.0006505i$	0.0005	$0.001 + 0.006505i$
	0.0252	0.6189	$0.0001 + 0.6189i$	0.6189	$0.001 + 0.6189i$

comes periodically close to TR_x (at the peaks where $|A_2|$ and $|A_3|$ are close to zero). The other peaks do not admit an interpretation as a basic wave. We observe that $|A_1(T)|$ and $|A_4(T)|$ as well as $|A_2(T)|$ and $|A_3(T)|$ have identical wave forms and a phase shift of π relative to each other.

For $0.025 < \alpha < 0.0251$ the orbit shown in Fig. 3(b) undergoes a period doubling cascade towards a chaotic attractor which persists for $0.0251 \leqslant \alpha \leqslant 0.02515$. The time series of the chaotic attractor are shown in Fig. 3(c) for $\alpha = 0.02515$. In Fig. 4(a), (b) and (c) we present the phase space plots of $|A_4|$ versus $|A_1|$ and $|A_3|$ versus $|A_2|$ for $\alpha = 0.025, 0.025025$ and 0.02515, respectively. When α increases further, we observe for $0.02515 < \alpha < 0.0252$ first a reverse period doubling cascade, then QP_2 again, and then, very close to 0.0252, QP_1. At $\alpha = 0.0252$, QP_1 is unstable again, and the travelling rectangle TR_x is the only attractor which remains so up to $\alpha = 0.026$. A time series demonstrating the approach to TR_x for $\alpha = 0.0252$ (for this value the approach is slow) is shown in Fig. 3(d).

Similar calculations for nearby values of r, $0.029 < r < 0.031$, show the same scenario, suggesting that the chaotic attractor occurs in a small "island" in the (r, α)-plane, surrounded by small concentric regions with quasiperiodic solutions that double their period when moving from the border to the center. We could, however, not find a structurally stable heteroclinic cycle in these simulations. A detailed analysis of the period doubling route to chaos is beyond the purpose of this paper and will be presented elsewhere. Although the scan has been done in a parameter range accessible to experiments, we believe that the experimental detection of the above scenario is challenging, due to the very narrow window in parameters space where it occurs.

5.3. Simulations of the GCCGLE

We have simulated the Ginzburg–Landau system (20), with the data fixed by the values calculated for the WEM parameters for which the normal form (21) shows a chaotic attractor (Eq. (22), $K_2 = 0.6875$, $K_3 = 1.25$, $r = 0.03$, $\alpha = 0.02515$). The parameters $a_0, a_1, \ldots, a_5$ are summarized in the third row of Table 2(a). The other parameters are (we use a scaling such that $d_{20r} = d_{02r} = 1$),

$$p_c = 1.0582, \quad q_c = 0.5053, \quad R_c = 9.0924, \quad \omega_c = 0.2282, \quad v_x = 0.0425, \quad v_y = 0.0462,$$
$$d_{20} = 1 + 0.0108i, \quad d_{21} = 0.4364 + 0.0149i, \quad d_{02} = 1 + 0.0275i.$$

In our simulations we use a Fourier–Galerkin approximation of the A_j, viewed as functions of (ξ, η, T) ($\xi = \xi_\pm$, $\eta = \eta_\pm$),

$$A_j(\xi, \eta, T) = \sum_{m=-M}^{M} \sum_{n=-N}^{N} a_j(m, n, T) e^{i(mr\xi + ns\eta)}, \quad 1 \leqslant j \leqslant 4. \tag{23}$$

Numerical convergence tests have shown that $M = N = 16$ is a reasonable choice to balance convergence and the computational efforts required by the global coupling terms and the size of the system. The ODE-system for the

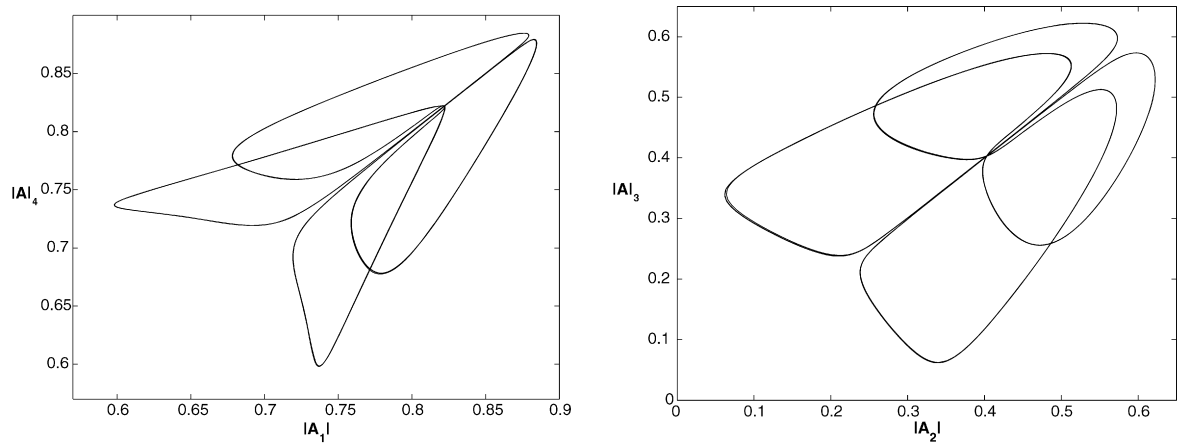

(a)

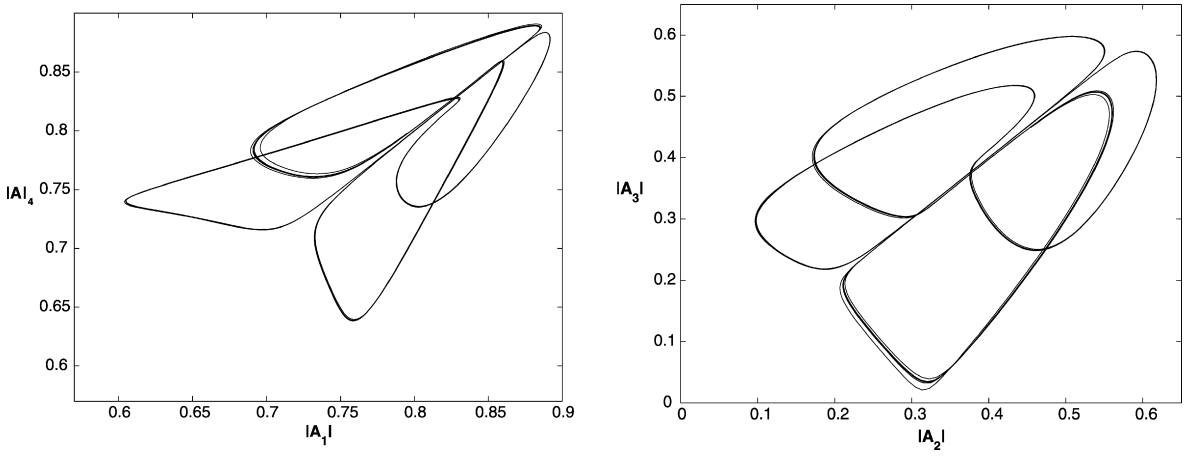

(b)

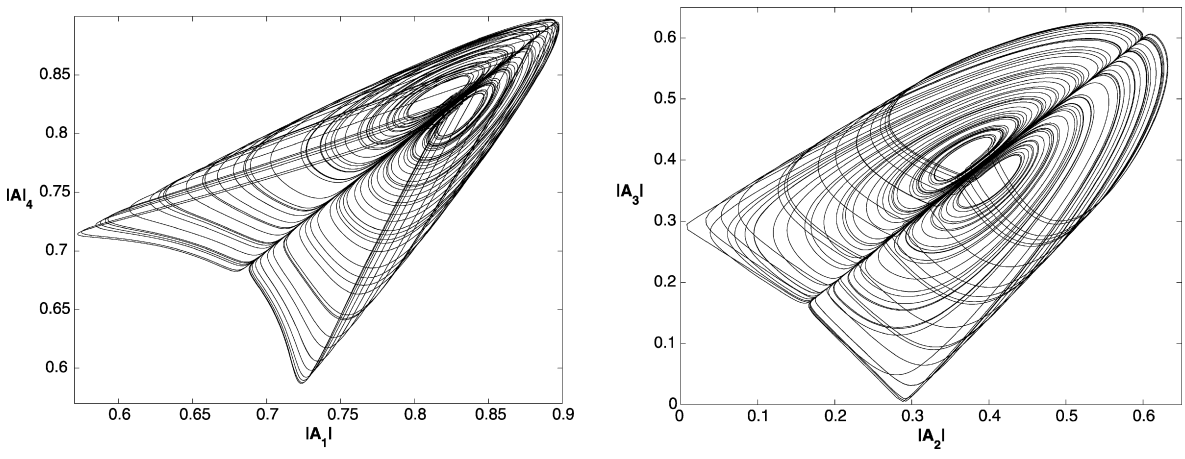

(c)

Fig. 4. Phase space plots of the quasiperiodic solutions and the chaotic attractor, for (a) $\alpha = 0.025$, (b) $\alpha = 0.025025$, and (c) $\alpha = 0.02515$ (see text).

mode amplitudes $a_j(m, n)$ is found by projecting (20) onto the modes kept in (23). The basic 'wave numbers' r, s are chosen such that the periodicity in (x, y) and the periodicity in (ξ, η) match for the given choice of ε. Given a numerical solution of (20) at time T, we can visualize the associated pattern by plotting

$$U(x,y,t) = \mathrm{Re}\big\{\big[A_1(\xi_+,\eta_+,T)e^{i(p_c x+q_c y)} + A_2(\xi_-,\eta_+,T)e^{i(-p_c x+q_c y)} + A_3(\xi_-,\eta_-,T)e^{i(-p_c x-q_c y)} + A_4(\xi_+,\eta_-,T)e^{i(p_c x-q_c y)}\big]e^{i\omega_c t}\big\}, \tag{24}$$

with $\xi_\pm = \varepsilon(x \pm v_x t)$, $\eta_\pm = \varepsilon(x \pm v_y t)$, $T = \varepsilon^2 t$. In our simulations we choose $\varepsilon = 0.2$.

We have run two simulations for the above parameters with two different initial conditions. In the following we describe the main features of the numerical solutions.

Simulation 1. In our first simulation we have chosen random initial values $|a_j(0,0,0)| < 1$ for the central modes, and small random perturbations $|a_j(m,n,0)| < 0.1$ $((m,n) \neq (0,0))$ for the non-central modes. To see which modes remain active in the long run, we computed temporal averages $< |a_j(m,n)| >$ over $0 \leqslant T \leqslant 1200$. The distribution of these averages is shown in Fig. 5(a) (with m,n shifted by ± 17 in order to separate them). We see that for $j = 2,3$ only the central modes remain active (average 0.3259 for both $j = 2$ and 3, the averages of all other modes are below 0.0087). For $j = 1,4$ the central modes are also dominant (averages 0.7110 for $j = 1$ and 0.7904 for $j = 4$), but in addition about eight other modes distributed to the left and right of the central modes are active (the averages of the neighboring modes are ≈ 0.24). Accordingly, A_2 and A_3 are approximately spatially uniform, whereas A_1 and A_4 are approximately translation invariant in the y-direction.

In Fig. 5(b) we show the real and imaginary parts and the absolute values of A_1 and A_4 as functions of x at $T = 1032$. Note that A_{1r} is strictly positive, and A_{1i} is strictly negative. For A_4 the situation is similar, except in intervals close to the endpoints $x = 0, 30$ (the unit of x in the plot is $2\pi/p_c$, and $30 \times 2\pi/p_c$-periodicity has been imposed in the x-direction). To demonstrate the spatiotemporal variation, we show in Fig. 5(c) horizontal space-time plots of A_{1r} and A_{4r} for $1032 \leqslant T \leqslant 1037$. In the dark (overlapping) regions of these plots the functions change their signs.

In Fig. 6 the snapshot at $T = 1032$ of the pattern U, Eq. (24), is shown. (In this and the other color-coded plots red is mapped to high and blue to low values. (For colors see the web version of this article.)) Here we can recognize regions dominated by approximative stripe patterns and regions dominated by approximative rectangular patterns. Generally, the spatial structure of the patterns observed in this simulation does not appear complex.

We observe, however, temporal complexity in the time series of all active mode amplitudes. In Fig. 7 (a) and (b) we show the time series of the absolute values of all central modes and of the next-to-central modes of A_1, A_4, respectively, for $0 \leqslant T \leqslant 20{,}000$. The dominant feature of the central mode time series are sharp "downwards" (close to zero) peaks occurring at apparently irregular times. In Fig. 7(c)–(f) four different phase space plots are shown. It is interesting to note that the plot of $|a_3(0,0)|$ versus $|a_2(0,0)|$ in Fig. 7(d) resembles the (right) plot of $|A_3|$ versus $|A_2|$ in Fig. 4(c), however, the plot of $|a_4(0,0)|$ versus $|a_1(0,0)|$ in Fig. 7(c) appears rather different from the (left) plot of $|A_4|$ versus $|A_1|$ in Fig. 4(c).

It appears that the temporal dynamics resulting from Simulation 1 is a kind of low-dimensional temporal chaos, reminiscent of the chaotic attractor of the normal form for the same values of the coefficients, but with a few additional modes being activated. We note that a similar type of low-dimensional spatiotemporal chaotic dynamics shown by (20), referred to as "zigzag-chaos", has been analyzed in some detail in [20].

Simulation 2. In our second simulation we chose fully random initial conditions. The resulting dynamics turned out to be radically different from that of Simulation 1, as is apparent in the temporal averages of the mode amplitudes shown in Fig. 8(a). Now A_1 and A_4 decay, whereas all modes of A_2 and A_3 remain active in the long run, indicating spatiotemporal complexity. The temporal complexity can be observed in the time series and phase space plots of the averages of $|a_2(m,n,T)|$ and $|a_3(m,n,T)|$ over (m,n) shown in Fig. 8 (b) and (c), respectively. The spatial complexity is revealed in the snapshots of A_{jr} and $|A_j|$, $j = 2,3$, shown in Fig. 9(a), as well as in the pattern snapshot displayed in Fig. 9(b). Note that at the blue spots in the plots of $|A_2|$ and $|A_3|$ the envelopes are approximately zero, corresponding to the "holes" observed already in simulations of a single 2d complex Ginzburg–Landau equation (see [28] for a recent review). The pattern in Fig. 9(b) is dominated by rectangles (for the normal form (21) the TR_x-solutions have the form $(A,0,0,A)$ or $(0,A,A,0)$), interlaced with dislocations leading to phase slips and grain boundaries.

In summary, the dynamics observed in this simulation appears temporally and spatially complex and may be identified with 'extensive spatiotemporal chaos'. Moreover, it coexists with the low-dimensional temporally chaotic but spatially ordered pattern described in the previous paragraph, for the same values of the parameters for which the normal form has a chaotic attractor and none of the basic waves is stable. A similar competition between ordered

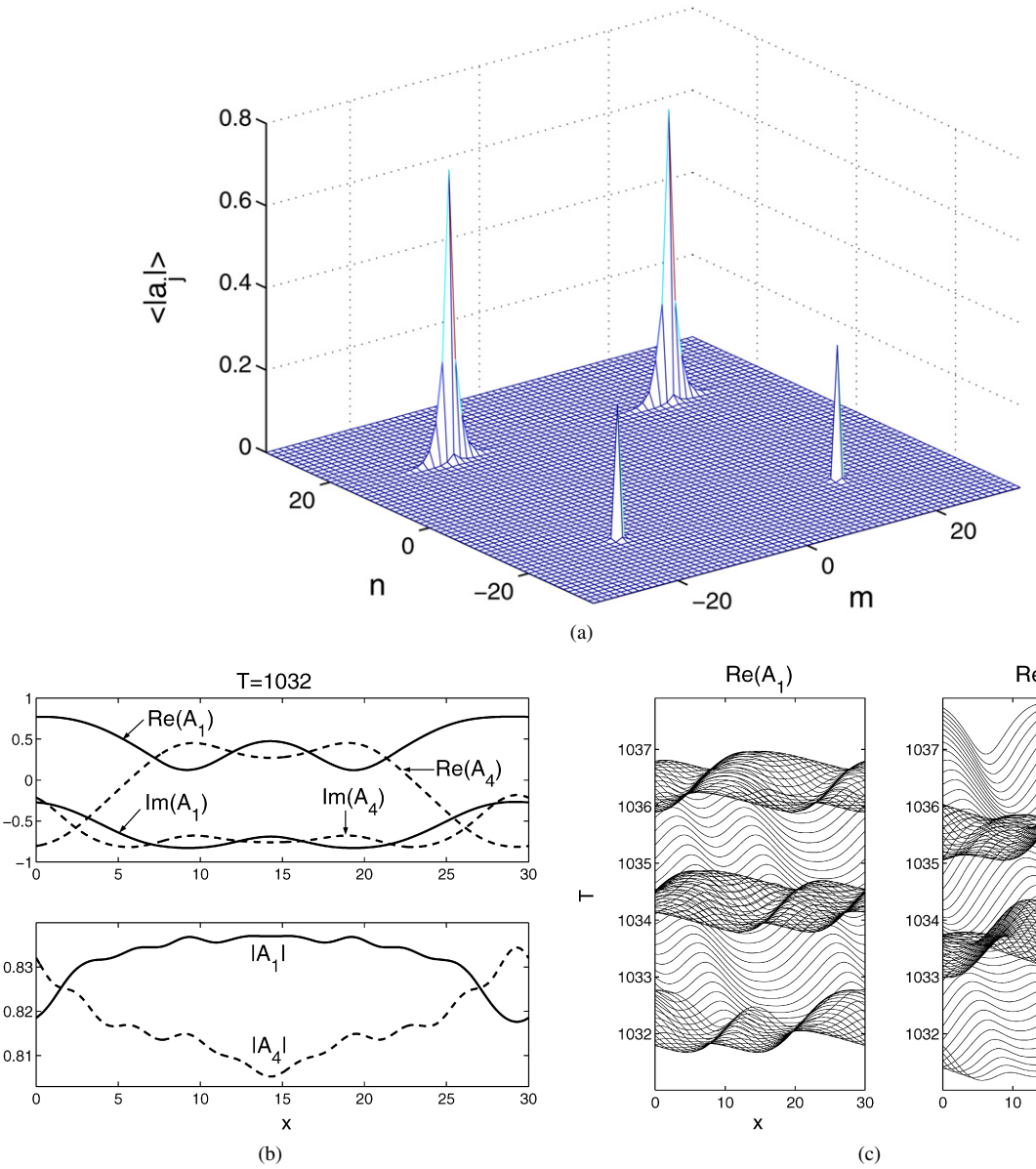

Fig. 5. Plots for Simulation 1. (a): Time averages of $|a_1(m-17, n-17, T)|$, $|a_2(m+17, n-17, T)|$, $|a_3(m+17, n+17, T)|$, and $|a_4(m-17, n+17, T)|$. (b): Horizontal cross sections of real and imaginary parts and absolute values of A_1 and A_4 at $T = 1032$. (c): Space–time plots $T_n + \mathrm{Re}(A_{1,4})$ versus x for $1032 \leqslant T_n \leqslant 1037$ and $T_{n+1} - T_n = 0.05$.

undulations and spatiotemporal undulation chaos has been observed recently in another anisotropic extended pattern forming system exhibiting spatiotemporal complexity, see [29] and references therein.

Based on the numerical simulations we conjecture here the existence of a temporal period doubling route towards the extensive spatiotemporal chaos, induced by the period doubling cascade observed in the normal form dynamics; a detailed analysis is beyond the scope of the paper.

5.4. Eckhaus stability boundaries

The basic wave solutions of (21) can be extended to families of basic wave solutions of the Ginzburg–Landau system (20), with continuously varying wave numbers centered around (p_c, q_c). If a basic wave solution is a stable

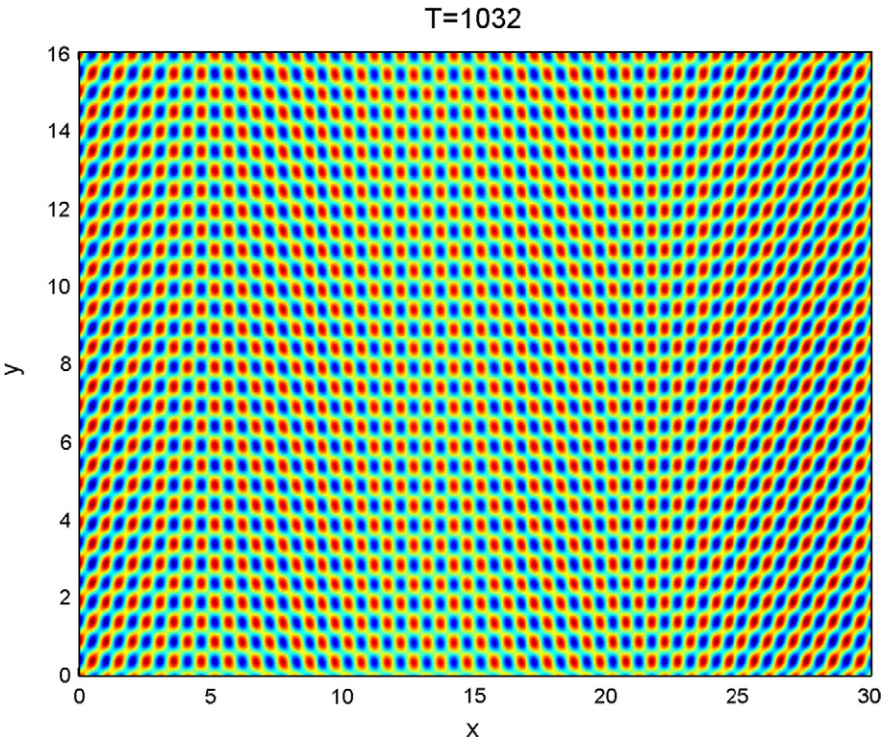

Fig. 6. Pattern snapshot U, Eq. (24), for Simulation 1 at $T = 1032$.

solution of (21), it can happen that all of the extended solutions are unstable solutions of (20), in which case we call the wave "Eckhaus unstable". On the other hand, if the wave with wave numbers (p_c, q_c) is a stable solution of (20), then there is a closed curve around (p_c, q_c) such that the waves inside that curve are stable, and the waves outside that curve are unstable solutions of (20). We refer to this curve as "Eckhaus stability" boundary (*ESB*). For each of the basic waves there are specific types of instabilities that can occur on an *ESB*. A systematic classification and analysis of all types of instabilities has been given so far only for the *TW*'s [25]. We have calculated the *ESB*-types for the parameters (r, α) in Fig. 1 for which the *TW* is a stable solution of (21). It turned out that in all cases a long wave (or phase) instability occurs, that is, the *TW*'s become unstable against perturbational *TW*'s with small wave numbers.

The analysis in Subsection 5.1 was for small values of (r, α), because such small values have been estimated for I52 [15]. For larger values of α we find again a region of stable waves, with "tongues" in the r-direction in which *TW* is a stable solution of (21). In this range different *ESB*-types can occur for *TW*. In Table 3(a) we summarize two parameter sets I, II for η_0–η_3, ϵ_a, σ_a, K_2, K_3, and α. The first seven parameter values of I and II are estimated values for I52 at 50 °C and 30 °C. For each of the two sets we varied r and determined the *ESB*-type of *TW* if it is a stable solution of (21). The results are summarized in Table 3(b). In this table, *EU*, E, E_t, and $E_t E$ stand for Eckhaus unstable, a long wave instability, a transverse instability, and both a long wave and transverse instability on the *ESB*, respectively. The *ESB*-type E_t is also a long wave instability, but against perturbations of another basic wave solution instead of *TW*. For some values of r the *TW* is subcritical, which is marked by an '*S*' in the table. For the set I and $r = 1.5$, *TW* is an unstable solution of (21) and only *AW* is stable. For the set II and $r = 1.3$, both *TW* and *AW* are stable solutions of (21), and the *ESB*-type of *TW* is $E_t E$.

6. Concluding remarks

We have presented an extensive bifurcation analysis of the weak electrolyte model for electroconvection of a layer of nematic liquid crystals, that allows for a systematic investigation of mechanisms generating the patterns observable experimentally. For the weakly nonlinear analysis we use four globally coupled complex Ginzburg–Landau

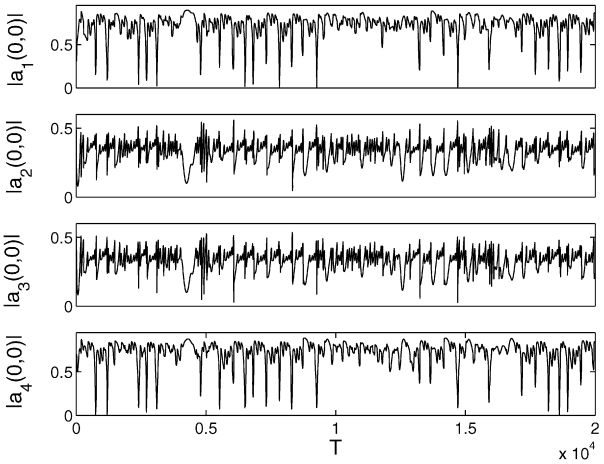

(a)

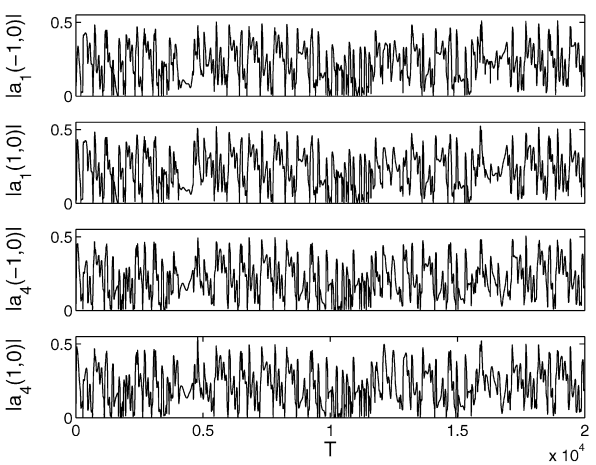

(b)

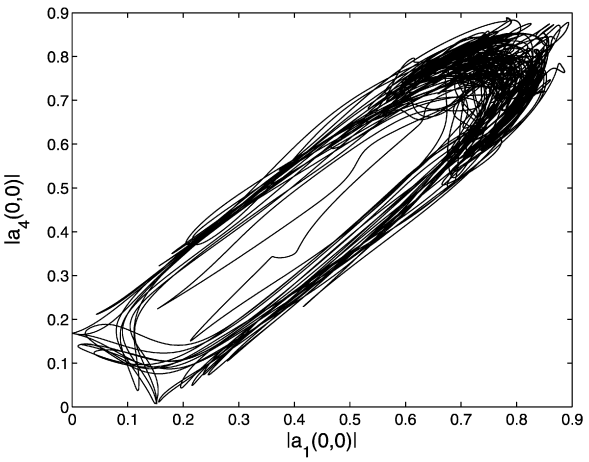

(c)

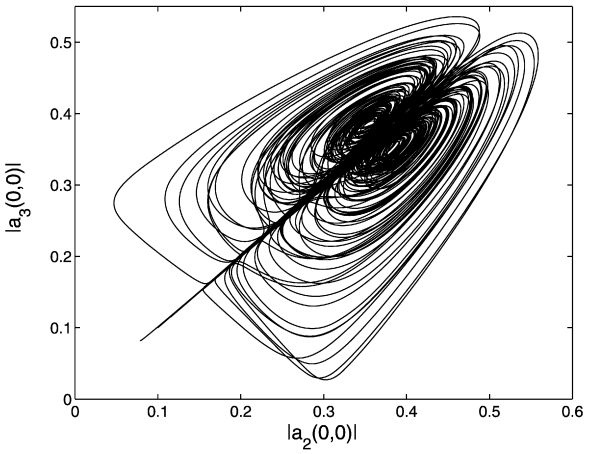

(d)

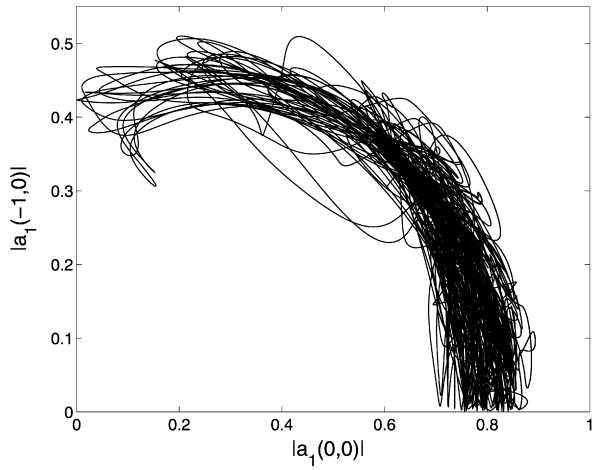

(e)

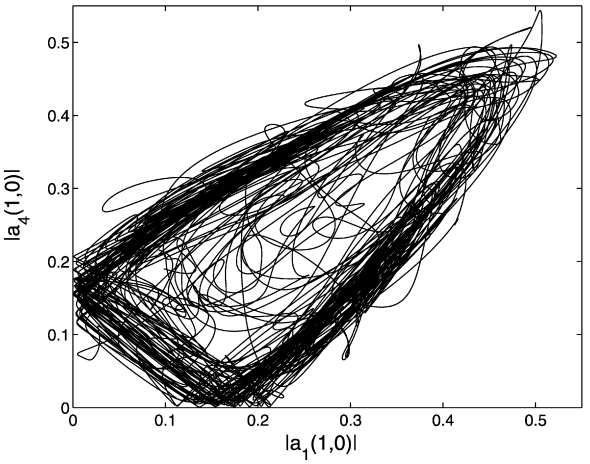

(f)

Fig. 7. Time series and phase space plots of dominant and secondary mode amplitudes plots for Simulation 1.

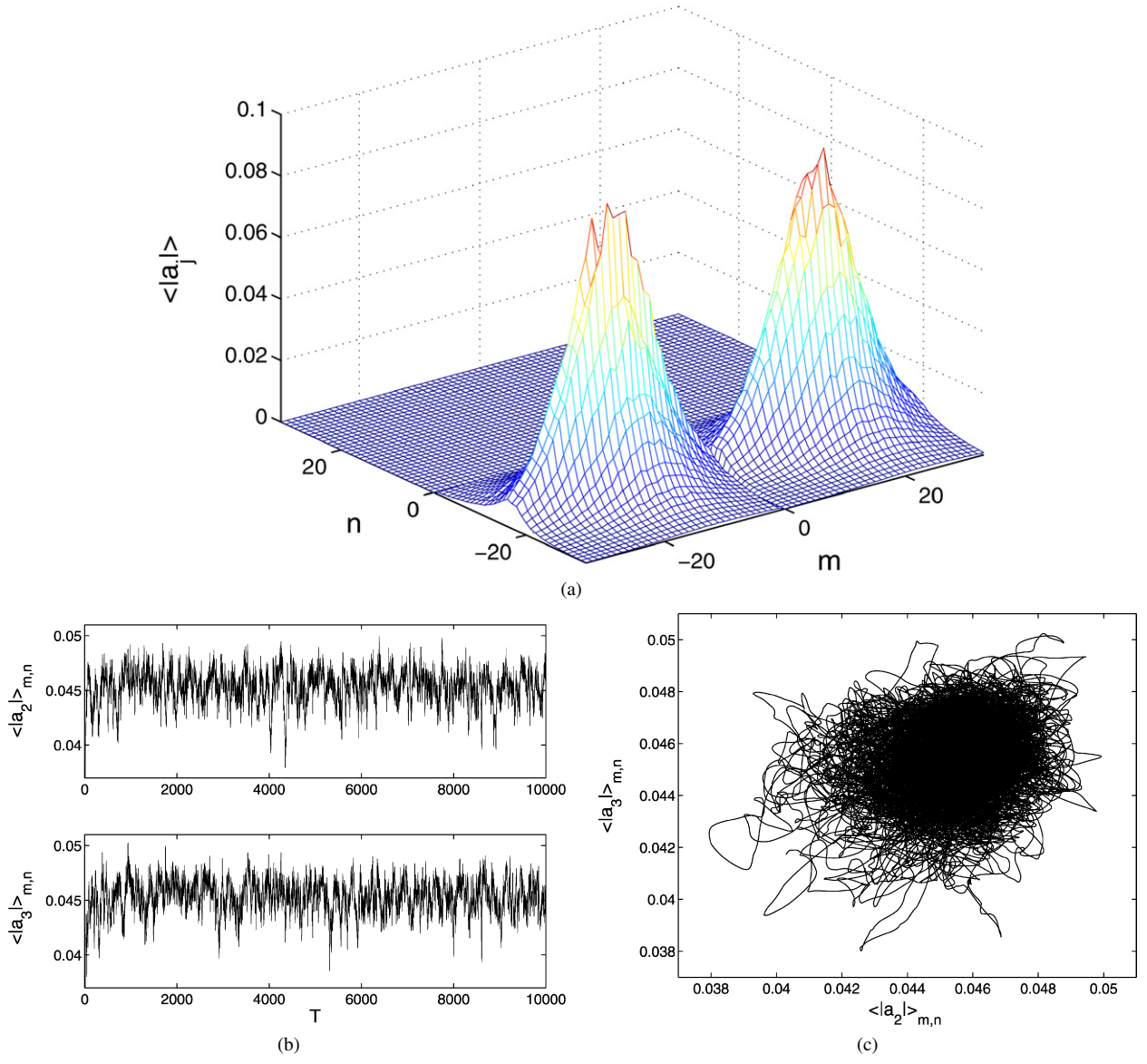

Fig. 8. Averages of the mode amplitudes $|a_j(m,n,T)|$ for Simulation 2. (a): Time averages. (b) and (c): Time series and phase space plots of the (m,n)-averages for $j=2,3$.

equations describing the dynamics of wave instabilities in two-dimensional anisotropic systems with translational and reflectional symmetry.

Inspired by the experiments confirming the weak electrolyte model, we investigated theoretically the pattern dynamics near the oblique Hopf bifurcation. Our results are in good agreement with previous computations [15]. In addition, we have found a rich variety of patterns at onset, such as travelling waves, standing rectangles and rolls, alternating waves, as well as more complex structures like low-dimensional spatiotemporal chaos and extensive spatiotemporal chaos dominated by holes, phase slips and grain boundaries, in different parameter regimes for the nematic Merck I52.

The analytical and numerical techniques developed in this paper allow the prediction of the types of the convective instability that can occur at the onset in experimentally accessible parameter regimes. In particular, the alternating wave structure predicted by our study has been recently observed in experiments [8]. We are currently investigating the possibility of exploiting these techniques to determine important but unknown physical parameters, such as the recombination rate.

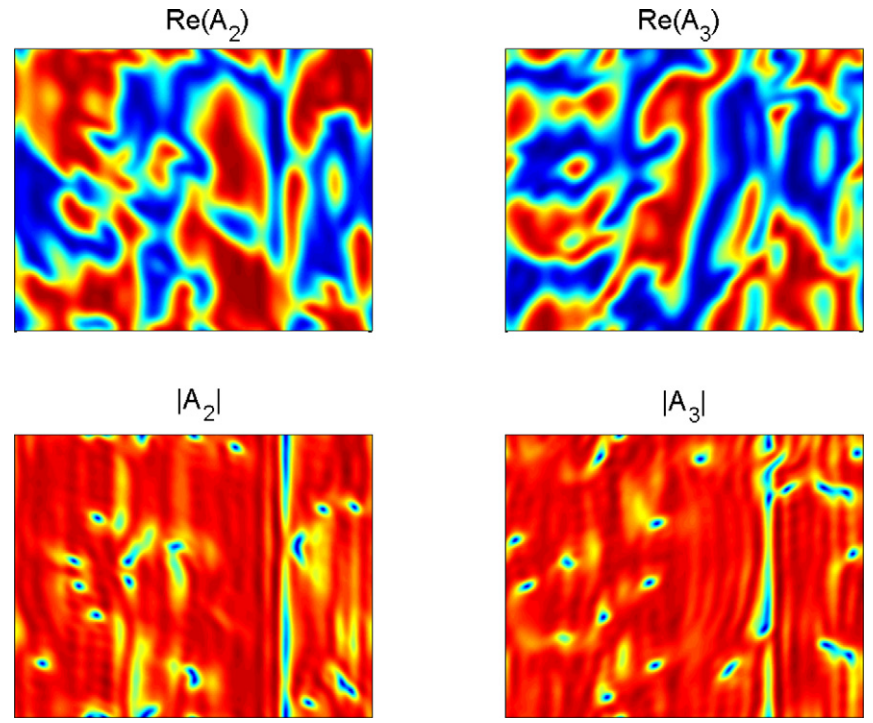

(a)

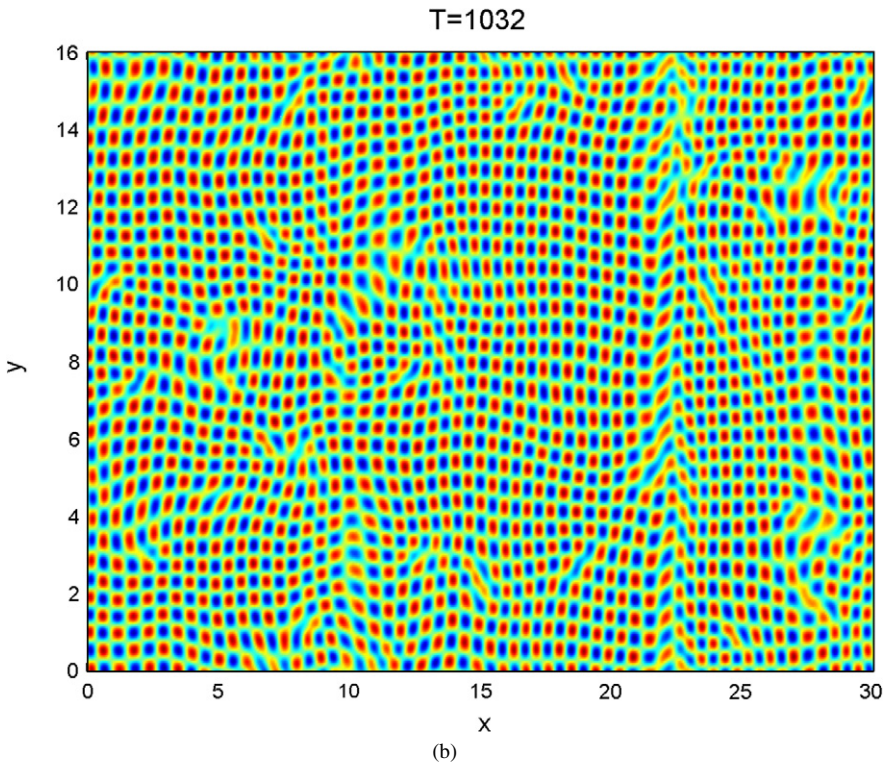

(b)

Fig. 9. Snapshots of (a): $\mathrm{Re}(A_j)$ and $|A_j|$ ($j = 2, 3$) and (b): pattern U, Eq. (24), for Simulation 2 at $T = 1032$. Scales in the upper figure are the same as in the lower figure.

Table 3
(a): Parameter sets I, II chosen for the *ESB* calculations for larger values of α. (b): ESB-types of *TW* when it is a stable solution of (21) for the sets I, II and a scan of r in the range $0.005 \leqslant r \leqslant 1.5$ (see text)

(a)		K_2	K_3	η_0	η_1	η_2	η_3	σ_a	ε_a	α
	I	0.6875	1.25	0.8115	0.8807	0.0807	0.1057	0.42	−0.0065	0.5
	II	0.6875	1.25	0.7913	0.8707	0.0707	0.0957	0.26	−0.0162	0.3

(b)	r	0.005–0.4	0.5	0.6	0.7	0.8	0.9	1	1.1	1.2	1.3	1.4	1.5
	I	*EU*	*E*	E_t	*EU*	*S*	*EU*	*EU*	*EU*	*S*	*EU*	*S*	*AW*
	II	*EU*	*EU*	*EU*	*EU*	*EU*	*EU*	*E*	*S*	*S*	$E_t E, AW$	*EU*	*EU*

Table 4
Coefficients c_p, c_q in $k_j^2 = c_p p^2 + c_q q^2$

	k_0^2	k_1^2	k_2^2	k_3^2	k_4^2	k_5^2	k_6^2	k_7^2	k_8^2
c_p	c	b	K_2	K_2	$1-\eta$	$(1-\eta)K_3$	$1+\varepsilon_a$	$1+\sigma_a$	$1+(1+\eta)\frac{\varepsilon_a}{2}$
c_q	b	c	1	K_3	$1+\eta$	$1+\eta$	1	1	1

	k_9^2	k_{10}^2	k_{11}^2	k_{12}^2
c_p	$c-(1+\eta)\frac{c\varepsilon_a}{2}$	$(1+\eta)cK_2+(1-\eta)(c-bK_2-cK_3)$	$(1+\eta)K_2+(1-\eta)(1-K_3)$	$(1+\eta)cK_2+(1-\eta)c$
c_q	b	$(1+\eta)c-(1-\eta)bK_3$	$1+\eta$	$(1+\eta)c+(1-\eta)bK_3$

In this paper we have considered the case of a constant external electrical field. Including *ac* fields in the model (with varying driving frequency of the external field), introduces another experimentally controllable bifurcation parameter. Moreover, the governing equations are then time-periodic, thus the model equations should be treated as a parametrically forced pattern formation system. We anticipate that by using Floquet theory the WEM equations are still tractable for the kind of analysis performed in this paper [30]. Away from resonances, the ODE normal form (21) as well as the GCCGLE (20) are then still valid generically. A similar bifurcation analysis for this case is under preparation and will be presented elsewhere.

Acknowledgements

We wish to thank to James Gleeson for valuable discussions. This research has been supported by the National Science Foundation under Grant No. DMS-0407418.

Appendix A

The linearized WEM equations depend on several anisotropic horizontal differential operators which become polynomials in (p, q) after Fourier transformation. To obtain a compact representation of these polynomials we introduce basic polynomials of the form $k_j^2 = c_p p^2 + c_q q^2$ $(0 \leqslant j \leqslant 12)$ in Table 4. The parameters a, b, c, η occurring in this table are defined by

$$a = \eta_0, \quad b = \frac{1}{4}\big[2(\eta_1+\eta_2) - (\eta_1-\eta_2)^2 - 1\big], \quad c = \eta_3, \quad \eta = \eta_2 - \eta_1.$$

With this notation the linearized equations for Σ, N_2, N_3 take the form (prime denotes ∂_z)

$$\partial_t \Sigma = -r\Sigma - ip\alpha^2\varepsilon_a R N_3' + \alpha^2\pi\sqrt{2R}/2(\partial_z^2 - k_6^2)\Phi', \tag{A.1}$$

$$\partial_t N_2 = (K_3\partial_z^2 - k_2^2)N_2 - iq(K_3-1)N_3' - (i/2)L_2(\mathbf{V}), \tag{A.2}$$

$$\partial_t N_3 = (1-K_3)iqN_2' + (\partial_z^2 + \varepsilon_a R - k_3^2)N_3 - \varepsilon_a\pi\sqrt{2R}/2ip\Phi - (1/2)L_3(\mathbf{V}), \tag{A.3}$$

where

$$L_2(\mathbf{V}) = (1+\eta)qV_1 - (1-\eta)pV_2, \qquad L_3(\mathbf{V}) = (1+\eta)V_1' - (1-\eta)ipV_3,$$

and the V_j are expressed through F, G as

$$V_1 = iqG + cipF', \quad V_2 = -ipG + biqF', \quad V_3 = k_0^2 F. \tag{A.4}$$

Note that (A.4) differs slightly from the commonly used representation of velocities in terms of stream functions. The chosen form turns out to be particularly useful when solving the nonhomogeneous velocity equations.

The linearized equation for the potential reads

$$(\partial_z^2 - k_7^2)\Phi - (\sqrt{2R}/\pi)(\sigma_a ipN_3 + \Sigma') = 0, \tag{A.5}$$

and the equations for the stream functions are given by

$$(k_0^4 k_1^2 - B\partial_z^2 + bck_0^2\partial_z^4)F - sp^3 qG' + \pi\sqrt{2R}(k_9^2\partial_z^2 - k_8^2 k_0^2)\Phi + L_F(N_2, N_3) = 0, \tag{A.6}$$

$$(A - k_0^2\partial_z^2)G + sp^3 qF' + \varepsilon_a \pi\sqrt{R/2}(1+\eta)pq\Phi' + L_G(N_2, N_3) = 0, \tag{A.7}$$

where $s = ac - 2bc - b^2 + c^2$, $A = bp^4 + (a - 2b + 2c)p^2q^2 + bq^4$, $B = c^2(a - 2b + 2c)p^4 + b(b^2 + 3c^2)p^2q^2 + 2cb^2q^4$, and

$$\begin{aligned} L_F(N_2, N_3) &= pq\big\{\big[(1+\eta)c - (1-\eta)K_3 b\big]\partial_z^2 - k_{10}^2\big\}N_2' - ip\big\{c(1+\eta)\partial_z^4 - \big[k_{12}^2 - (1+\eta)c\varepsilon_a R\big]\partial_z^2 \\ &\quad + \big[(1-\eta)k_3^2 + (1+\eta)\varepsilon_a R\big]k_0^2\big\}N_3, \\ L_G(N_2, N_3) &= (k_2^2 k_4^2 - k_5^2\partial_z^2)N_2 + iq\big[(1+\eta)(\partial_z^2 + \varepsilon_a R) - k_{11}^2\big]N_3'. \end{aligned}$$

Appendix B

In this appendix we summarize in Table 5 typical critical values found in our linear stability analysis of the WEM.

Table 5
Critical values R_c, p_c, q_c, associated Hopf frequencies ω_c, and critical group velocities v_x, v_y for $r = 0.02$ and α from 0.02 to 0.035, with the other parameters given by (22) and (a) $K_2 = 0.6053$, $K_3 = 1.2105$, (b) $K_2 = 0.6875$, $K_3 = 1.25$, and (c) $K_2 = 0.875$, $K_3 = 1.25$, as in the calculations for Fig. 1

(a)	α	p_c	q_c	R_c	ω_c	v_x	v_y
	0.020	0.9635	0.8638	8.2722	0.1805	0.0331	0.0270
	0.025	0.9643	0.8642	8.2807	0.2263	0.0413	0.0337
	0.030	0.9652	0.8646	8.2905	0.2719	0.0495	0.0403
	0.035	0.9663	0.8651	8.3017	0.3176	0.0578	0.0469
(b)	α	p_c	q_c	R_c	ω_c	v_x	v_y
	0.020	0.9839	0.7791	8.6698	0.1854	0.0331	0.0303
	0.025	0.9848	0.7795	8.6787	0.2321	0.0414	0.0377
	0.030	0.9857	0.7800	8.6892	0.2788	0.0497	0.0452
	0.035	0.9868	0.7804	8.7010	0.3254	0.0580	0.0527
(c)	α	p_c	q_c	R_c	ω_c	v_x	v_y
	0.020	1.0559	0.5027	9.0651	0.1821	0.0336	0.0367
	0.025	1.0568	0.5029	9.0744	0.2280	0.0420	0.0458
	0.030	1.0579	0.5031	9.0853	0.2739	0.0504	0.0549
	0.035	1.0591	0.5034	9.0975	0.3199	0.0589	0.0640

References

[1] L. Kramer, W. Pesch, Convection instabilities in nematic liquid crystals, in: H. Hoffmann, M. Schwoerer, T. Vogtmann (Eds.), Macromolecular Systems: Microscopic Interactions and Macroscopic Properties, Wiley, 2000, pp. 250–294.

[2] W. Pesch, U. Behn, Electrohydrodynamic convection in nematic, in: F.H. Busse, S. Müller (Eds.), Evolution of Spontaneous Structures in Dissipative Continuous Systems, Springer-Verlag, Berlin, 1998, pp. 335–383.

[3] A. Buka, N. Éber, W. Pesch, Convective patterns in liquid crystals driven by electric field, Liquid Crystal Commun. (2005) 1–21 (electronic), http://www.e-lc.org/docs/2005_07_12_04_29_54.

[4] S. Chandrasekhar, Liquid Crystals, University Press, Cambridge, 1977.
[5] M. Dennin, G. Ahlers, D.S. Cannell, Spatiotemporal chaos in electroconvection, Science 272 (1996) 388.
[6] M. Dennin, G. Ahlers, D.S. Cannell, Chaotic localized states near the onset of electroconvection, Phys. Rev. Lett. 77 (1996) 2475.
[7] J.T. Gleeson, Sustained spatiotemporal chaotic flow at onset of electroconvection in nematic liquid crystals, Physica A 239 (1997) 211.
[8] G. Dangelmayr, J. Gleeson, G. Acharya, I. Oprea, J. Ladd, Diagnosis of spatiotemporal chaos in wave-envelopes of an electroconvection pattern, in preparation, 2008.
[9] E.F. Carr, Influence of electric fields on the molecular alignment in the liquid crystal p-(anisalamino)-phenil acetate, Mol. Cryst. Liqu. Cryst. 7 (1969) 253–269.
[10] W. Helfrich, Conduction-induced alignment of nematic liquid crystals: basic model and stability considerations, J. Chem. Phys. 51 (1969) 4092–4105.
[11] W. Zimmermann, L. Kramer, Oblique-roll electrodynamic in nematics, Phys. Rev. Lett. 55 (1985) 402.
[12] M. Dennin, A study in pattern formation: Electroconvection in nematic liquid crystals, PhD Thesis, Department of Physics, University of California, Santa Barbara, 1995.
[13] M. Treiber, L. Kramer, Bipolar electrodiffusion model for electroconvection in nematics, Mol. Cryst. Liqu. Cryst. 261 (1995) 311.
[14] M. Dennin, M. Treiber, L. Kramer, G. Ahlers, D.S. Cannell, Origin of traveling rolls in electroconvection of nematic liquid crystals, Phys. Rev. Lett. 76 (1996) 319.
[15] M. Treiber, On the theory of the electrohydrodynamic instability in nematic liquid crystals near onset, PhD Thesis, University of Bayreuth, 1996.
[16] M. Treiber, L. Kramer, Coupled complex Ginzburg–Landau equations for the weak electrolyte model of electroconvection, Phys. Rev. E 58 (1998) 1973.
[17] G. Dangelmayr, M. Wegelin, Hopf bifurcations in anisotropic systems, in: M. Golubitsky, D. Luss, S. Strogatz (Eds.), Pattern Formation in Continuous and Coupled Systems, in: IMA Vol. Math. Appl., vol. 115, 1999, pp. 33–42.
[18] G. Dangelmayr, B. Fiedler, K. Kirchgässner, A. Mielke, Dynamics of Nonlinear Waves in Dissipative Systems: Reduction, Bifurcation and Stability, Addison-Wesley Longman Ltd., 1996.
[19] G. Dangelmayr, L. Kramer, Mathematical tools for pattern formation, in: F.H. Busse, S. Müller (Eds.), Evolution of Spontaneous Structures in Dissipative Continuous Systems, Springer-Verlag, Berlin, 1998, pp. 1–85.
[20] I. Oprea, I. Triandaf, G. Dangelmayr, I.B. Schwartz, Quantitative and qualitative characterization of zigzag spatiotemporal chaos in a system of amplitude equations for nematic electroconvection, Chaos 17 (2007) 023101.
[21] B. Werner, Numerical computation of degenerate Hopf bifurcation points, ZAMM 78 (1998) 807–821.
[22] E. Allgower, K. Georg, I. Oprea, G. Dangelmayr, Matrix-free numerical computation of instabilities of periodic patterns, in: G. Dangelmayr, I. Oprea (Eds.), Dynamics and Bifurcation of Patterns in Dissipative Systems, in: World Scientific Series on Nonlinear Sciences, Series B, World Scientific Publisher, 2004, pp. 20–38.
[23] M. Silber, H. Riecke, L. Kramer, Symmetry breaking Hopf bifurcation in anisotropic systems, Physica D 61 (1992) 260.
[24] M. Wegelin, Nichtlineare Dynamik raumzeitlicher Muster in hierarchischen Systemen, PhD Dissertation, Department of Physics, Tubingen, 1993.
[25] G. Dangelmayr, I. Oprea, Modulational stability of travelling waves in 2D anisotropic systems, J. Nonlinear Sci. 18 (1) (2008) 1–56.
[26] G. Dangelmayr, I. Oprea, A bifurcation study of wave patterns for electroconvection in nematic liquid crystals, Mol. Cryst. Liqu. Cryst. 413 (2004) 2441.
[27] J.H. Swift, Hopf bifurcation with the symmetry of the square, Nonlinearity 1 (1988) 333–377.
[28] J. Lega, Phase diffusion and weak turbulence, in: G. Dangelmayr, I. Oprea (Eds.), Dynamics and Bifurcation of Patterns in Dissipative Systems, in: World Scientific Series on Nonlinear Sciences, Series B, World Scientific Publisher, 2004, pp. 157–183.
[29] K.E. Daniels, O. Brausch, W. Pesch, E. Bodenschatz, Competition and bistability of ordered undulations and undulation chaos in inclined layer convection, J. Fluid. Mech. 57 (2008) 261–282.
[30] G. Schneider, H. Uecker, The amplitude equations for the first instability of electroconvection in nematic liquid crystals in case of two unbounded space directions, Nonlinearity 20 (2007) 1361–1386.